EUROPEAN SOUTHERN OBSERVATORY

Organisation Européenne pour des Recherches Astronomiques dans l'Hémisphère Austral
Europäische Organisation für astronomische Forschung in der südlichen Hemisphäre

Report:
FORS Zero Point Monitoring
And
Absolute Photometry

VLT-TRE-ESO-13112-5429

Issue: 2.0

Date: 12/12/2012

Prepared:	Daniel Bramich, Wolfram Freudling	12/12/2012		
	Name	Date		Signature
	Lodovico Coccato, Palle Møller	12/12/2012		
	Name	Date		Signature
	Sabine Moehler, Carlo Izzo	12/12/2012		
	Name	Date		Signature
Approved:	Martino Romaniello	17.12.12		
	Name	Date		Signature
Released:	Martino Romaniello	17.12.12		
	Name	Date		Signature
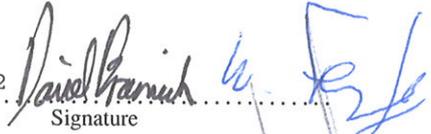
Change Record

Issue	Date	Sections Affected	Remarks
1.0	23/09/2011	All	Document creation
2.0	12/12/2012	All	General updates; Updated phrasing of calibration plan (Section 5.2)

Executive Summary

The FORS photometric zero point has been monitored for quality control (QC) purposes for many years. As part of the FORS Absolute Photometry (FAP) project (Freudling et al. 2006), we have investigated how the photometric zero point, atmospheric extinction coefficients and colour term coefficients can be used for the absolute photometric calibration of FORS2 images. Specifically, in this document, we: (i) report on our verification work of the FORS2 imaging pipeline (Section 2 & Appendix A), (ii) describe how we fixed a major bug in the standard star identification algorithm (Section 3), (iii) analyse the effect of different standard star observing strategies (with the aid of detailed simulations) on the precision to which we can monitor the photometric zero point and atmospheric extinction, and the absolute photometric accuracy that is achievable by FORS2 (Section 4), and (iv) provide the necessary recommendations in order to design and implement a suitable calibration plan[1] (Section 5).

The **key findings with regard to the monitoring of the photometric zero point** are as follows:

- The **photometric zero points computed for QC monitoring** are calculated using average extinction coefficients (usually for the previous period), which means that they **correlate with the airmass and the true extinction coefficient of the observations**. Correctly computed zero points are independent of the airmass and extinction of the observations (see also Freudling & Bramich 2009).

- From December 2009 to April 2011, the algorithm for identifying standard stars failed in ∼40% of all cases, and a fall-back algorithm was employed which itself was not reliable. This lead to **QC zero points being computed from random stars in the field mistaken to be standard stars**. These errors, mixed in with correctly measured standard stars, introduced subtle systematic errors in the zero points that were delivered, resulting in a set of plausible zero points that did not actually reflect the real photometric zero point of the instrument.

- The investigation into the standard star misidentification problem yielded measurements of the orientation of FORS2 images on the sky, and the analysis of these data lead to the important conclusion that **blind offset acquisition should be limited to less than 60″** (Freudling, Bramich & Møller 2011).

These algorithmic problems have been fixed, and a full set of tested recipes are now available to compute algorithmically-correct photometric zero points that are useful both for QC monitoring and scientific photometric calibration.

The **key findings with regard to the observational strategy for obtaining data on photometric standard stars** are as follows:

- The **current procedure used at Paranal to collect photometric calibration standards provides too few data points** to monitor the long term stability of the photometric zero point, to derive reliable nightly extinction coefficients, or to allow an absolute photometric calibration accuracy of better than 3%.

- The **standard star fields were not well selected during observing** to provide calibrating stars with a homogeneous range of colours due to a lack of appropriate guidelines. New recommendations for standard star fields to be observed at different times of the year have been prepared and are tabulated in this document.

- The FORS2 user manual (Saviane 2010) describes **a photometric calibration plan that does not match with the procedural instructions** in place at Paranal (see Appendix B).

- These **procedural instructions have not been followed properly in terms of the number of stars observed in photometric nights. This failure has not been detected** during the normal course of operations. Standard star data that satisfy the criteria of the new calibration plan are essential to achieving our monitoring and calibration goals, and therefore we must implement a system that alerts PSO when the calibration plan is not being followed, in order to avoid the undesirable situation that insufficient calibration data is available.

The **key findings with regard to the testing of the FORS2 imaging pipeline** are as follows:

---

[1]The implementation of the calibration plan developed in this document will be presented in a separate document by Ivo Saviane.

- **The FORS2 imaging pipeline was found to be well-developed and well-documented, and the algorithms were found to be performing correctly**, with only minor issues with the data reduction being identified.

- **The FORS2 imaging pipeline is almost compliant with the Science Grade Data Products (SGDP) standard**, which requires physical units, full error propagation, science headers and optimal signal-to-noise. Some work still needs to be done in this respect (e.g. photometric zero points should be propagated to the FORS2 image headers) and we plan to submit a proposal to the Data Products Board (DPB) to bring the FORS2 imaging pipeline to the SGDP standard.

Recommended Actions

We recommend that the following actions are taken:

1. Adopt the new calibration plan proposed in Section 5.2 of this document including our specifications as to which standard star fields should be observed throughout the course of the year (Section 5.3). This might require effort to modify the software for generating the relevant observing blocks (OBs).

2. Implement QC monitoring of the fulfillment of the new calibration plan with a feedback loop to Paranal operations to flag any failures that are detected. This might be done as part of the `calchecker` procedure.

3. Finish implementing and testing the QC monitoring procedure for the photometric zero point and nightly extinction coefficients using the data from the implementation of the new calibration plan.

4. Implement the use of correctly computed extinction coefficients from standard star images at the beginning of the night to aid in judging the photometric quality of the night. For this purpose, regular updates of the photometric zero point will be required which should be used by Paranal.

5. Submit a proposal to the DPB to: (i) discuss the minor data reduction issues in the FORS2 imaging pipeline and decide on actions, (ii) bring the FORS2 imaging pipeline to the SGDP standard, and (iii) to use the data collected by following the new calibration plan for further investigation into the possibility of fitting and applying an illumination correction.

6. Review consistency and/or update all documentation on FORS2 photometry, in particular the FORS2 calibration plan in the FORS2 user manual, the procedural instructions for FORS2 observers, the call for proposals, and the P2PP manuals.

Contents

1 Introduction

ESO's definition of a photometric night is that extinction variations within such a night are less than 2% (Silva 2007). The FORS Absolute Photometry (FAP) project aims to provide tools to let users take advantage of photometric nights and routinely achieve 3% photometric accuracy, and even better accuracy when additional calibrations are collected. In previous work, we have investigated the feasibility to achieve this accuracy. The status of the FAP project when our current work was initiated was as follows:

- A combination of static and rotating illumination patterns had been found in the FORS2 twilight flat field images (Møller et al. 2005; Freudling et al. 2006; Moehler et al. 2010). Consequently, the FAP project team proposed a procedure to collect the data required to calibrate photometry affected by these systematic errors in the flat fielding.

- A procedure for correcting systematic photometric errors introduced by a static flat field illumination pattern had been implemented as a FORS2 pipeline recipe called `fors_photometry`. However, this recipe had not yet been scientifically validated.

In this phase of the work for the FAP project, our initial aim was to analyse the standard star data that had been collected over the last few years in order to develop and test a system for calibrating the systematic photometric errors introduced into the photometry by the static and rotating illumination patterns in the FORS2 sky flats. However, we found a number of other issues that needed resolving before such work could be undertaken, and this report details the findings from our investigation and the analysis of these issues, including a description of the solutions that were implemented.

The report concentrates on describing our investigations into the use of the FORS2 imaging pipeline for processing standard star observations to monitor the photometric zero point of the instrument and the extinction above Paranal, and then using these derived quantities to calibrate the photometry of the FORS2 science observations. During this work, we have verified that the pipeline algorithms employed in performing the photometry are producing reliable results (see Section 2), while fixing a major bug in the standard star identification algorithm that was found during the course of this work (see Section 3). Then, based on the standard star fields that we currently observe from the Stetson catalogue (Stetson 2000; Stetson 2007) and the signal-to-noise (S/N) of the photometry that we obtain from these standard star images, we have characterised how the distribution of such observations over airmass and time impacts the precision to which we can monitor the photometric zero point and atmospheric extinction coefficient, and consequently how this impacts the absolute photometric accuracy that is achievable by FORS2 (see Section 4). By requiring that we can monitor the photometric zero point and atmospheric extinction coefficient to precisions of $\sim$1% and $\sim$10%, respectively, and by requiring that we can reach an absolute photometric accuracy of 3% with the FORS2 instrument, we have been able to translate our findings into an observing and modelling strategy that should be followed in order to achieve these constraints.

In Section 5, we present a detailed proposal for a new calibration plan that will achieve the monitoring and calibration goals stated in Section 4.1, while optimising the use of the Stetson standard star fields that are visible in the sky throughout the night at different times of the year. The data from the new calibration plan will also enable the desired further investigation into correcting the systematic photometric errors introduced into the photometry by the static and rotating illumination patterns in the FORS2 sky flats.

2 FORS2 Imaging Pipeline Verification

The FORS2 imaging pipeline consists of a small number of recipes that run in sequence to process the imaging data into a set of instrumental photometric measurements for the objects in the field. For a standard star image, the reduction cascade consists of the recipes `fors_bias`, `fors_img_sky_flat` and `fors_zeropoint`. For a science image, the reduction cascade consists of the recipes `fors_bias`, `fors_img_sky_flat` and `fors_img_science`. Optional processing steps may involve the recipes `fors_dark` and `fors_img_screen_flat`, but these are rarely used for standard star or science image processing. A further recipe `fors_photometry` is available for multi-image analysis of standard star data, and our verification work for this recipe in particular is described in Ap-

pendix A. Hence we have concentrated our verification work on the four recipes `fors_bias`, `fors_img_sky_flat`, `fors_zeropoint` and `fors_img_science`.

Our work on the verification of the FORS2 imaging pipeline started with version 4.8.5, and ended with version 4.9.7. As with the UVES pipeline (see Section 2 of Bramich & Freudling 2012), in our verification work we aimed to test the following:

- Verify the reduction cascade inputs and outputs, and check the documentation of such.

- Verify the recipe input parameters, their range of validity, and the robustness of each recipe with respect to the values of the input parameters.

- Understand the function of each recipe input parameter and its effect on the data products at each stage.

- Check that the recipe input parameters are clearly described and documented.

- Understand the algorithms implemented in each pipeline recipe, and check that they are documented clearly in the pipeline manual.

- Determine the results/products that need checking in order to verify the quality of the results from each recipe.

- Determine how to optimise the quality of the final photometry, including the maximisation of S/N.

Without a `Reflex` workflow to streamline the data organisation and scripting of the pipeline recipes, we were forced to test the pipeline recipes on small sets of associated data supplied by the Data Processing and Quality Control group (QC group). However, these data sets were sufficient to perform the basic verifications required.

We used the `Remedy` ticketing system to log and track the bugs/issues we found with the pipeline recipes. To summarise, we submitted 9 tickets which break down into 3 small bugs (*DFS10236* - SOLVED; *DFS10241* - SOLVED; *DFS10244* - SUSPENDED) and 1 major bug (*DFS10270* - SOLVED - see Section 3), and requests for necessary pipeline improvement (*DFS10366* - SOLVED), new documentation (*DFS10288* - SOLVED; *DFS10456* - SOLVED), further development (*DFS10289* - SUSPENDED) and to hide unnecessary parameters (in a similar manner to the UVES pipeline; *DFS10266* - SOLVED).

However, the vast majority of our tests did not find any problems with the quality of the results from the pipeline recipes, or the documentation of such. A full list of the tests that we performed is beyond the scope of this report and we limit ourselves to highlighting the two most important tests pertinent to the quality of the scientific products. Both tests demonstrate that the photometry produced by the FORS2 pipeline does not from suffer systematic errors relative to the photometry produced by other independent software packages.

Firstly, we have verified that the aperture photometry performed by `fors_zeropoint` (via a call to the `SExtractor` software - Bertin & Arnouts 1996) produces instrumental magnitude measurements of the sources in an image that are fully consistent with similar independent measurements performed manually via the `IRAF` routine `phot`. By "fully consistent", we mean that for a set of stars S, where the ith star has a standard magnitude M_i and magnitude measurements $m_{1,i}$ and $m_{2,i}$ from each independent reduction, the scatter in the quantities $(m_{1,i} - M_i)$ and $(m_{2,i} - M_i)$ is comparable as a function of standard magnitude, *and* that, for the bright stars $j \in S$, the difference $(m_{1,j} - m_{2,j})$ is approximately zero (i.e. the residuals $(m_{1,j} - M_j)$ have the same sign and amplitude as the residuals $(m_{2,j} - M_j)$).

Secondly, we confirm that the CCD noise model adopted in the FORS2 pipeline is correct, and that it implements full frame error propagation in the correct fashion, including the generation and propagation of error frames associated with the calibration frames. This is a highly desirable feature in any data reduction pipeline in order to provide reliable estimates of the uncertainties on the quantities supplied in the data products for the pipeline. As a further test of the adopted CCD noise model in the FORS2 pipeline, we compared the uncertainties on the instrumental magnitude measurements from `fors_zeropoint` with the corresponding uncertainties reported by `IRAF` using the routine `phot` and employing two separate noise estimation methods at the pixel level (a purely analytical method similar to `fors_zeropoint` and a semi-empirical method) to generate the noise model. As expected, we find that the `fors_zeropoint` and `IRAF` instrumental magnitude uncertainties are consistent with each other (although such uncertainties are heavily underestimated at the bright end for various reasons - see Section 4.2).
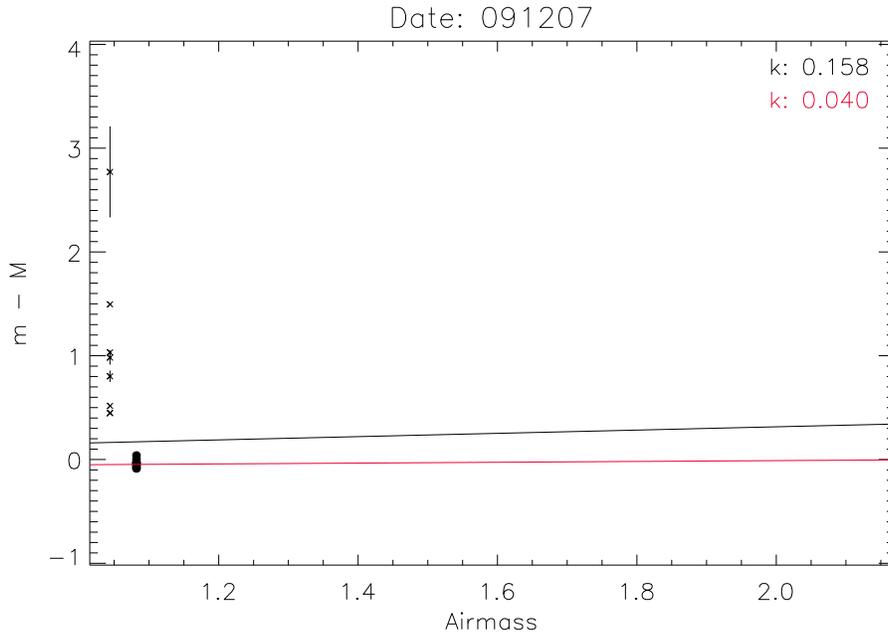
Figure 1: Plot of instrumental magnitude measurements minus the corresponding standard magnitudes and the fitted zero point versus airmass for all standard star observations on the night of 20091207 for the R filter and detector 1. Note that the fit includes data from a number of different nights, but only the data for one of the nights is shown. The black line represents the part of the fitted long-term photometric model that corresponds to the data in this plot (ignoring the small contribution from the colour term), and the red line represents the same model after iteration to remove outliers. Corresponding extinction coefficients in units of mag/airmass are reported in the upper right hand corner of the plot.

3   Performing Robust Standard Star Identification In The FORS2 Pipeline

As reported in the ticket *DFS10270*, during the FORS2 imaging pipeline verification it was discovered that the recipe `fors_zeropoint` was misidentifying the standard stars from the Stetson catalogue in an image for a significant fraction ($\sim$2-5%) of input images. In this Section, we briefly describe how this problem was detected and how we developed and implemented a more robust algorithm for standard star identification.

3.1   Residuals Of Fits To FORS2 Standard Star Photometric Data

During the development work for the current phase of the FAP project, we experimented with fitting a long-term photometric model on a per filter and per detector basis to the instrumental magnitude measurements of all standard stars observed in the four month period from December 2009 to March 2010. The data were taken from the QC archive which stores the results of the QC reductions of the raw standard star images up to the end of the `fors_zeropoint` recipe. The long-term photometric model that we adopted consists of a single photometric zero point, an extinction coefficient for each night on which a standard star image was obtained, and a single colour term coefficient (see Section 4.1 for more details). The aim was to extract a reliable set of measurements of the atmospheric extinction coefficient per filter and to plot them as a function of time.

As part of the model fitting process, we inspected the fit for each filter and detector on each night with observations. For example, in Figure 1, we plot the instrumental magnitude measurements minus the corresponding standard magnitudes and the fitted zero point versus airmass for all standard star observations on the night of 20091207 for the R filter and detector 1. The observations on this night, in this filter and for this detector consist of two standard star images, from which we obtain a photometric measurement of each standard star in each image, taken at different airmasses of $\sim$1.04 and $\sim$1.08, which explains the clustering of data points into two vertical lines. The part of the fitted model

8

corresponding to the data in this plot (ignoring the small contribution from the colour term) is represented by the black line, and the reported extinction coefficient for this night (and filter) is perfectly plausible at ∼0.158 mag/airmass.

However, it is clear that the data from the image at airmass ∼1.04 are highly scattered over more than 2 magnitudes along the vertical axis in contrast to the well-clustered data at airmass ∼1.08 and to the expected scatter consistent with the photometric uncertainties of the order of ∼1-5%, which indicates the presence of serious systematic errors. Iteration of the fit for the long-term photometric model results in the rejection of all the data points from the image at airmass ∼1.04, and the new fit (red line) now passes neatly through the data at airmass ∼1.08, yielding another plausible extinction coefficient of ∼0.040 mag/airmass. The rejection of these data points also indicates their status as outliers. Similar data with a large scatter and numerous outliers occur in the photometry from ∼2-5% of the images that we considered for use in the fit. Clearly the effect of such data is disastrous for the measurement of an accurate extinction coefficient, sometimes resulting in an unphysical measurement (i.e. a negative value), and furthermore, such data serve to introduce subtle systematic errors in the derived photometric zero point.

3.2 Misidentification Of Standard Stars

Concerned about the problematic pipeline photometry described in Section 3.1, we launched an investigation into the cause of the large photometric scatter. Inspection of the pipeline logs for the known cases highlighted the fact that the pattern matching method being used to derive the coordinate transformation between the world coordinate system (WCS) of the standard star image and the Stetson catalogue WCS was failing to find a solution and that a "fall-back" method for standard star identification was being used instead. We also linked the occurrence of the large photometric scatter with images where the offset between the image WCS and the Stetson catalogue WCS is generally greater than ∼10 pix, indicating that the telescope pointing was in error by greater than ∼2.5″.

The fall-back method employed by `fors_zeropoint` for identifying the standard stars in an image is a very simple algorithm that assumes that the WCS of the standard star image is accurate (to within a few unbinned pixels). It works by determining which standard stars from the catalogue should lie in the image field-of-view based on the image WCS and then matches each of these standard stars with the *nearest* detected star in the image. Clearly, if the image WCS is accurate (and the coordinates of the standard stars in the catalogue are correct), then the standard stars will be matched with the correct stars in the image. However, if the image WCS suffers a systematic error such as an offset or rotation, then there is a substantial risk that the nearest detected star in the image is *not* the correct standard star.

In fact, when the pattern matching fails, and the image WCS is systematically in error, we find that the fall-back method for standard star identification generally misidentifies most or all of the standard stars in the field, with the majority of the misidentifications occurring when the observed star field is crowded and/or when the image WCS is least accurate. The pattern matching failure and image WCS error occur for ∼2-5% of standard star images (depending on the filter under consideration) which is perfectly consistent with the fraction of images yielding a large scatter in the standard star photometry.

As an illustrative example, consider the standard star image from detector 1 for the R filter corresponding to the photometry at airmass ∼1.04 as discussed in Section 3.1. This image is displayed in Figure 2 as the image in the background. The green circles in this image represent the expected positions of the USNO-B stars in this field based on the USNO-B catalogue coordinates and the image WCS. It is clear that the expected catalogue star positions are systematically offset from the real star positions in the image by the same vector of length ∼40 pix. Since the USNO-B catalogue coordinates do not suffer from such an error, the image WCS derived from the telescope pointing must be the source of the error.

In the same image, the black circles indicate which stars are identified by `fors_zeropoint` as standard stars. Comparison of this set of stars with the standard stars marked by black circles in the finding chart for this field (foreground image in Figure 2) reveals that each standard star has been misidentified in the standard star image as a result of the recipe having matched the nearest detected star to the expected standard star pixel coordinates. Consequently, the instrumental magnitude measurement assigned to each standard star suffers a systematic error equal to the difference in magnitude between the misidentified star and the standard star in question, which can easily be as large as ∼1-5 mag and that is different for each standard star under consideration. This is clearly the cause of the large photometric scatter in this example.
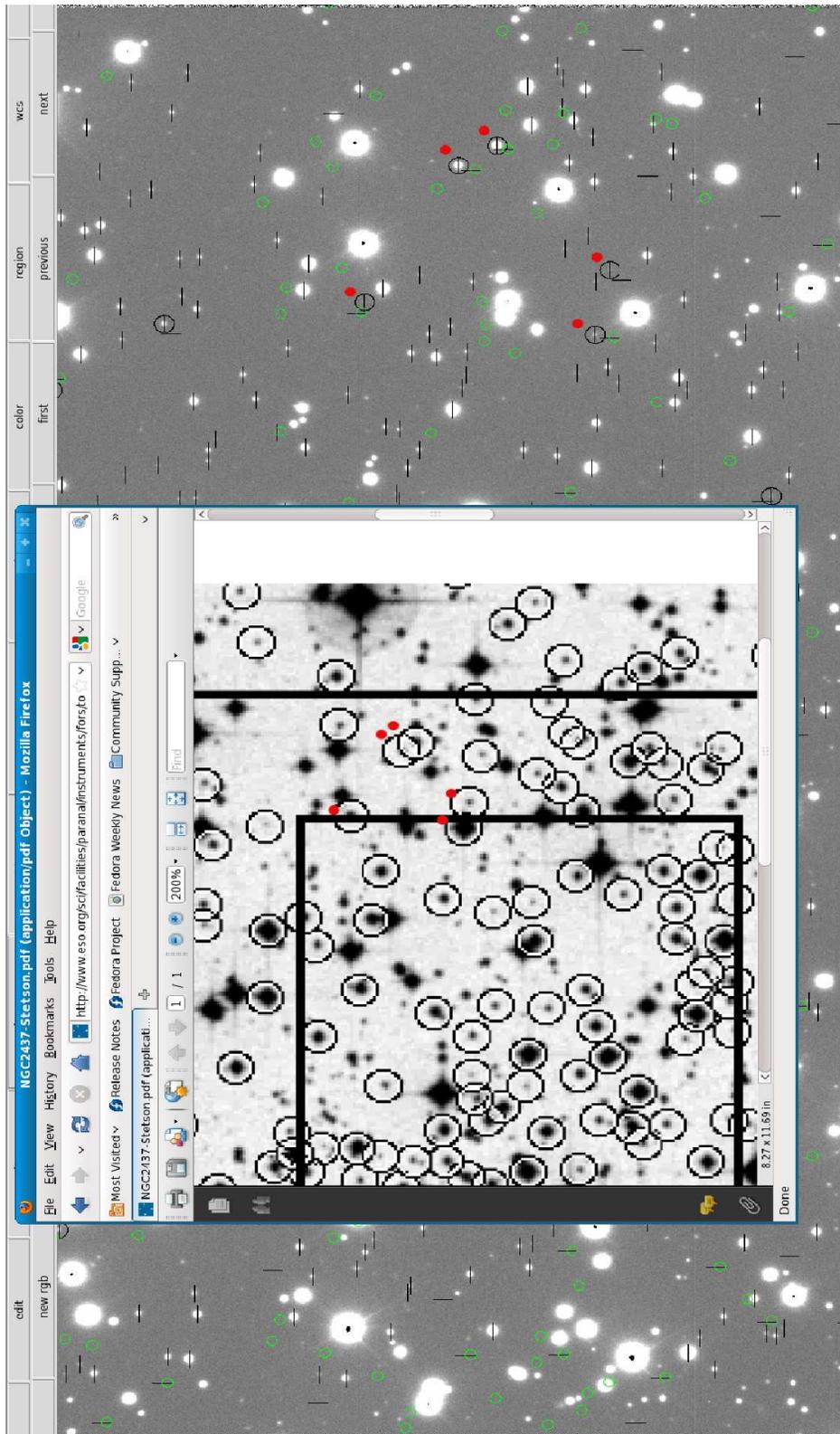
Figure 2: **Background image:** The standard star image corresponding to the photometry at airmass ∼1.04 as discussed in Section 3.1. The green circles represent the expected positions of the USNO-B stars in this field based on the USNO-B catalogue coordinates and the image WCS. The black circles indicate which stars are identified by fors_zeropoint as standard stars. **Foreground image:** The finding chart for the Stetson standard stars in this field. The black circles indicate which stars are standard stars. **Both images:** Red dots have been plotted to help draw the eye to specific examples of standard star misidentification.

3.3 Failing Pattern Matching And Data Quality Issues

On investigation of the pattern matching method being employed by `fors_zeropoint`, which is a customised implementation of the Valdes et al. (1995) triangle matching algorithm, we found that it was failing to find a solution for the coordinate transformation between the image and the catalogue for ∼40% of input standard star images. Independent tests using an implementation of the more robust Pál & Bakos (2006) triangle matching algorithm also exhibited a similar failure rate, suggesting that the reason for the failure of the triangle matching in `fors_zeropoint` was not due to an algorithmic error. We note that these well-studied algorithms usually enjoy a success rate of well above 99% for astronomical images containing at least three stars with Gaussian-like PSFs and a reasonable S/N. We suspect that the main reasons for failure are due to poor data suitability/quality for use in the pattern matching algorithms. This conclusion is supported by the fact that for a large proportion of the standard star images where the pattern matching method was failing, there are very few standard stars in the field-of-view and/or the telescope active optics are disabled so as not to saturate the brighter standard stars resulting in a ring-like (non-Gaussian-like) image PSF unsuitable for star detection and centroiding (but still suitable for aperture photometry).

Since we have demonstrated in Section 3.2 that the fall-back method employed by `fors_zeropoint` for identifying the standard stars is flawed, we have removed this method from the recipe. However, we are left with the problem that the pattern matching method employed by `fors_zeropoint` is failing ∼40% of the time mainly due to the attempted processing of data of insufficient quality for this algorithm. This makes it desirable to develop a more robust method for standard star identification that can successfully process the standard star data of poorer quality (few standard stars, or non-Gaussian-like PSF, etc.) and hence we have also disabled the pattern matching method in `fors_zeropoint`.

3.4 A Robust Shift Determination Method

The pattern matching algorithm in `fors_zeropoint` deals with trying to find a solution for the coordinate transformation between the coordinate systems of the image and of the standard star catalogue, and the triangle matching implementation is suitable for coordinate systems related by any non-singular combination of shifts, rotations and scale changes. However, this treatment is overly complicated given that the image WCS and catalogue WCS are related by a simple two-dimensional translation (rotation is small at ∼0.08 deg, equivalent to a deviation of ∼5 unbinned pixels (or ∼1.25″) over the area of the FORS2 detector - see Freudling, Bramich & Møller (2011)). Therefore, the new algorithm for standard star identification should be concerned with determining the two-dimensional translation between the coordinate systems in a robust manner. For this purpose, we choose to use a cross-correlation technique as the basis of the algorithm.

Consider a set of objects A with known coordinates in a coordinate system S_A and another set of objects B with known coordinates in a coordinate system S_B, and assume that at least some of the objects in A are common to the set of objects in B. This set up may be interpreted as A being the set of objects detected in a standard star image with image pixel coordinates determined via an object detection routine, and B being the set of standard stars from a relevant catalogue with corresponding image pixel coordinates derived using the catalogue celestial coordinates and the image WCS. Let us also make the further assumption that S_A and S_B are related by a simple translation, corresponding to our situation for FORS2 images. Then, for each object in B, one may calculate the x and y pixel offsets to each object in A, resulting in a data set of $N_A N_B$ pixel offsets (dx_i, dy_i), where N_A and N_B are the number of objects in A and B, respectively.

We note that for each object in B that is also an object in A, there will be a single calculated pixel offset that is a valid estimate of the coordinate shift (dX, dY) between S_A and S_B. Therefore, if there are M objects in B that are also in A, then there will be M estimates of (dX, dY) in the set of pixel offsets (dx_i, dy_i). All of the remaining calculated pixel offsets will be distributed randomly according to the spatial distribution of the objects in A and B.

Now consider a two-dimensional histogram of the set of (dx_i, dy_i) values (limited to the area of a FORS2 image) with a bin size equal to 1 pix². Assuming that the size of the coordinate shift (dX, dY) between S_A and S_B is smaller than the size of a FORS2 image, then the histogram peak value will be ∼ M for the bin to which (dX, dY) belongs since the typical scatter in the (dx_i, dy_i) measurements of ∼0.01-0.1 pix is much smaller than the histogram bin size. Furthermore, assuming an approximately uniform spatial distribution of objects in the field with $N_A \approx N_B \approx 100$, then there will be ∼$10^4$ pixel offset measurements spread uniformly over the histogram area of ∼2000×4000 pix (the

size of an unbinned FORS2 detector), implying that most of the histogram bins will have a value of zero with an average of approximately one in 10^3 bins having a value of 1. We also note that the probability that a histogram bin randomly attains a value of 2 is $\sim 10^{-6}$, which implies that there will only be ~ 8 such bins for a $\sim 2000 \times 4000$ pix histogram. Further similar analysis reveals that we do not expect a histogram bin to randomly attain a value of 3 for FORS2 images.

Hence, by constructing the histogram described above, one may obtain an estimate of (dX, dY) to within an accuracy of ~ 1 pixel by searching for the peak histogram bin, and this peak (with value $\sim M$) is highly likely to be unique when there are at least three objects in common between A and B. By limiting the histogram area to $\sim 200 \times 200$ pix, which easily encompasses the vast majority of coordinate shifts between the image WCS and catalogue WCS for FORS2, then, for only two objects in common between A and B, the peak histogram bin should also be unique and correspond to (dX, dY). This algorithm is intrinsically more robust than pattern matching when rotations and scale changes can be neglected, because pattern matching includes the unnecessary free parameters relating to rotations and scale changes.

An important potential problem with this method is the effect of rotation. If there is a non-negligible rotation between S_A and S_B, then the above method will not work. Even small rotations of 0.05-1 deg have a noticeable effect on increasing the spread in the M measurements of (dx_i, dy_i) that estimate (dX, dY) between S_A and S_B, which leads to a smaller amplitude and wider peak in the two-dimensional histogram. This problem may be avoided for small rotations by increasing the bin size appropriately so that a single histogram bin encompasses the expected range in the (dX, dY) estimates over the area of the FORS2 detector, although one must be aware that by increasing the bin size it becomes more likely that any single bin may randomly attain a larger value. This of course is not an issue when there are a reasonable number of objects in common between A and B, but it could become a problem if there are only two or three such objects.

3.5 Algorithmic Implementation

Based on the method described in Section 3.4 and the associated discussion, we have implemented an algorithm for standard star identification in a standard star image in the recipe `fors_zeropoint`. The algorithm implementation performs the following steps on an image from a single detector:

1. Reads in the Stetson standard star catalogue and converts the standard star coordinates to image pixel coordinates using the WCS in the image header.

2. Extracts the subset of standard stars that are expected to lie in the field-of-view of the image under consideration. If there are no such standard stars, then a failure is declared.

3. Performs object detection and analysis in the image using `SExtractor`.

4. For each standard star in the subset of relevant standard stars, the algorithm calculates x and y pixel offsets to all detected objects in the image.

5. Constructs a two-dimensional histogram of the x and y pixel offsets calculated for all standard stars in step (4). The bin size is set to one square image pixel, and the histogram is constructed over the domain $-150 < dx < 150$ pix and $-150 < dy < 150$ pix since we do not expect a systematic offset between the image WCS and the catalogue WCS of more than ~ 50 pix.

6. Calculates the maximum value of the histogram. If the maximum value is zero because all of the histogram bin values are zero, then a failure is declared.

7. Determines the number of peaks in the histogram that attain the maximum histogram value. We define such a maximal-peak as a set of spatially connected histogram bins that attain the maximum histogram value.

8. If there is more than one maximal-peak in the histogram, then the histogram is recalculated with a bin size of nine square image pixels (i.e. it is binned 3×3), and steps (6) and (7) are repeated. If there is still more than one maximal-peak in the histogram, then a failure is declared.

9. Calculates the centroid of the unique maximal-peak in the histogram using a 3×3 box centred on the maximal-peak. The coordinates of the centroid of the maximal-peak in the histogram are adopted as the estimate of the offset (pix) between the image WCS and the catalogue WCS.

10. Applies the offset derived in step (9) to the image pixel coordinates of the subset of relevant standard stars. Then, for each of these standard stars, the algorithm selects the closest detected object in the image with a centroid within 5 pix of the corrected standard star coordinates as the object corresponding to the standard star in question, with the possibility that no such detected object exists. If this results in no standard star matches with detected objects, then a failure is declared.

The `fors_zeropoint` recipe writes out the histogram of pixel offsets constructed in step (5) as a FITS file for possible inspection by the user. In Figure 3 we reproduce an interesting selection of these histograms from our test data.

In order to verify that the new method of standard star identification in FORS2 images works properly, we manually checked the identifications for a small set of test images of different standard star fields with varying numbers of standard stars, and with a range of stellar crowding and PSF quality. These preliminary tests were encouraging in that most images were successfully processed, and such images did not suffer from a single standard star misidentification. Images for which the algorithm failed were simply declared as recipe failures and did not produce any results. For the example standard star image discussed in Section 3.2, all standard stars in this field were correctly identified by the new algorithm.

Hence we proceeded to download all 4642 FORS2 standard star images and their associated calibrations taken between December 2009 and April 2011 for use in a full verification and characterisation of the new algorithm. We reduced the data using the intermediate version 4.9.1 of the FORS2 pipeline with default parameters, employing the recipes `fors_bias` and `fors_img_sky_flat`, and the modified recipe `fors_zeropoint`. We found that for 215 image pairs (one image from each detector; ∼9.3%), the recipe `fors_zeropoint` failed to identify any standard stars for one or both detectors. Investigation of these failures revealed that approximately half of them are due to poor data quality (instrument rotation, wrong field observed, poor image PSF, etc.), and that for the remainder there are too few standard stars in the field to produce a unique maximal-peak in the histogram of pixel offsets.

We also assessed the rate of incorrect determinations of the coordinate offset between the image WCS and the catalogue WCS, since it is these cases which may result in standard star misidentifications. We did this by checking for inconsistent offsets derived for both detectors in any one image pair. We found 15 such image pairs (∼0.6%) where the derived coordinate offset was different for each detector, although investigation into these cases revealed that 14 image pairs suffered from a rotation of ∼0.7 deg between the image WCS and catalogue WCS, a previously discovered problem for images from the period 24/01/2010 to 02/02/2010. For the remaining image pair, we could not find a reason for the inconsistency between the detectors in the derived coordinate offsets, which implies that the new algorithm only yields an incorrect offset for <0.05% of input images.

We therefore conclude that the new standard star identification algorithm based on the analysis of the histogram of candidate coordinate offsets enjoys a high success rate with FORS2 imaging data (>90%, compared to ∼60% for the original pattern matching algorithm), and it is extremely robust in the sense that failures to find the standard stars are caught and such data are then simply discarded. Furthermore, standard star misidentification happens only in the rarest of cases (<0.05% of images). The modifications described in this Section are available in version 4.9.1 and later of the FORS2 pipeline.

4 Simulating Standard Star Observations

In this Section, we describe a set of simulations of standard star observations that we have performed with the aim of determining the preferred observing strategy in order to minimise the amount of scientific integration time used on these observations while providing useful constraints on the photometric zero point, the nightly atmospheric extinction coefficients, and the systematic photometric error that may be introduced by applying a photometric calibration derived from the standard star observations.
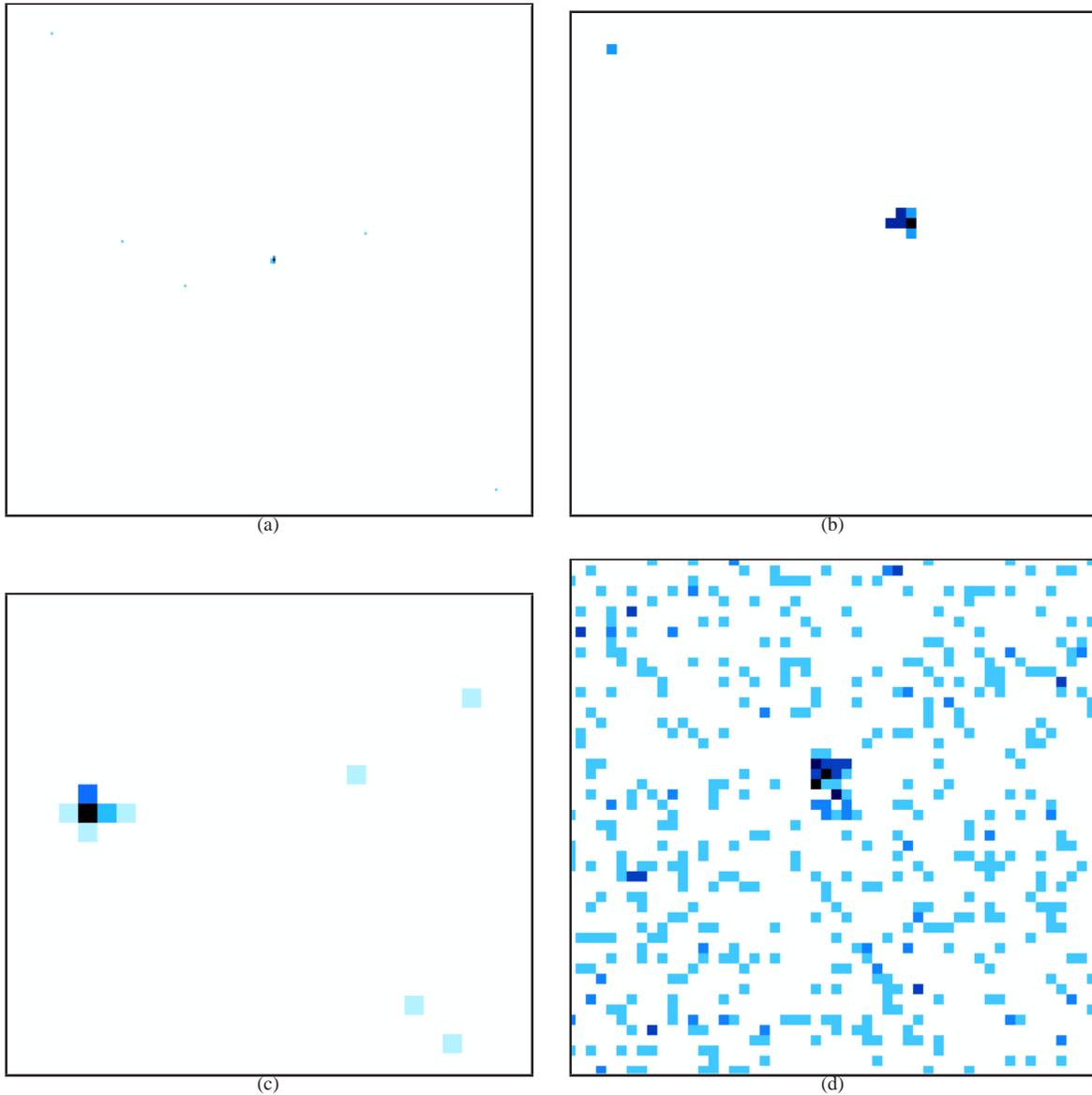
Figure 3: Example histograms of the x and y pixel offsets calculated for the standard stars in step (4) of the algorithm described in Section 3.5. In each case, the image colour scale runs through the blue colour channel from white for values of zero to black for the maximum histogram value. **(a):** A typical full $301{\times}301$ bin histogram that attains a maximum value of 6 in a single bin lying in the cluster of non-zero bins near the centre of the histogram. The majority of the histogram bins have values of zero, with a few randomly scattered bins containing a value of 1. **(b):** A zoomed-in view of the central region of another typical histogram. The maximum value is 3 in the single black bin. **(c):** Similar to (b) except that the histogram is even more magnified and the maximum bin value in this case is 13. **(d):** This histogram corresponds to an image with a small 0.7 deg rotation between the image WCS and the catalogue WCS. The rotation has had the effect of widening and reducing the peak at the correct coordinate offset, which can be seen as the conglomeration of non-zero bins near the centre of the histogram. In fact, this histogram has already been further binned $3{\times}3$ as described in step (8) because the original higher-resolution histogram had more than one maximal-peak, and this further processing has resulted in a single maximal-peak with a value of 5 in each of two spatially connected bins. Note that the relatively high density of histogram bins with values of 1, 2 or 3 spread across the histogram area is due to the combination of the larger bin size for this histogram and the fact that the corresponding image is of a relatively crowded star field.

4.1 Purpose Of The Simulations

The FAP project aims to provide the user with the ability (in principle when observing with sufficient S/N) to reach an absolute photometric accuracy of 3% with the FORS2 instrument for science imaging observations (Freudling et al. 2006) through the establishment of observational requirements for the calibrating standard stars and a methodology for analysis of the standard star data once obtained.

Images of standard star fields are obtained as part of the instrumental calibration plan, and they are processed through the FORS2 imaging pipeline to correct for bias level and flat field patterns to produce calibrated images. Aperture photometry is performed on the objects that are detected in the calibrated images using a fixed aperture of radius 7″in order to measure the total object flux for each object (with no aperture losses). The standard stars from the Stetson catalogue that lie in the field of view are matched with the detected objects in the calibrated images (using the method described and implemented in Sections 3.4 & 3.5), and the instrumental magnitude measurements are recorded in a photometric table along with the standard star identifications and the corresponding catalogue magnitudes.

On collection of a series of standard star images in a single filter (and from a single detector), it becomes possible to fit the set of instrumental magnitudes of the standard stars with a photometric model such as:

$$\overline{m}_i = M_p + Z + k_j X_i + a(M_p - M'_p) \tag{1}$$

where $\overline{m}_i$ is the model magnitude for the ith instrumental magnitude measurement m_i in the bandpass under consideration, M_p and $(M_p - M'_p)$ are the standard magnitude and colour corresponding to the pth standard star for which m_i was measured, Z is the photometric zero point of the instrumental system, k_j is the extinction coefficient (mag/airmass) for the jth observational grouping to which m_i belongs (we assume from now on that each night is photometrically stable and that images may therefore be grouped by night of observation), X_i is the airmass of the observation, and a is the colour-term coefficient.[2]

The parameters of the model presented in Equation 1 provide an important description of the detector+instrument+telescope optical properties and the properties of the atmosphere during the observational epochs. Namely, the photometric zero point Z gives a measure of the sensitivity of the detector+instrument+telescope system, and it can be monitored over time to check for degradation of the instrument performance, and the extinction coefficient(s) k_j provide a measure of the atmospheric transparency, which is closely linked to whether a night may be considered photometric or not. It is therefore desirable to obtain standard star observations that constrain the coefficients Z, k_j and a to a required precision for instrumental and atmospheric monitoring. For our monitoring purposes, it is desirable to achieve uncertainties of ∼1% (or 0.01 mag), ∼10% and ∼10% in the coefficients Z, k_j and a since the instrumental throughput degradations (e.g. due to dust on the mirror) are of the order of a few percent, and classification of a night as photometric requires an assessment of the stability of the extinction coefficient over the night.

Furthermore, the fitting of the model in Equation 1 is the first step in calibrating the instrumental magnitude measurements of the scientific objects of interest, for which standard magnitudes and colours will (most likely) not be known. To calibrate an instrumental magnitude measurement of a science object to a standard magnitude, inversion of Equation 1 is required,[3] and any errors in the coefficients Z, k_j and a will affect the accuracy of the derived standard magnitude. As stated at the beginning of this Section, we aim to be able to achieve ∼3% photometric accuracy with FORS2, and therefore the uncertainties on the calibration coefficients Z, k_j and a should be small enough to produce systematic errors of less than 3% when calibrating instrumental magnitudes of science objects, even if this necessitates standard star observations that yield calibration coefficients with precisions that are better than those that we require for our monitoring purposes.

It is clear then that we are interested in optimising our standard star observations to be able to obtain a target precision on the parameters of interest Z, k_j and a, and to minimise the systematic error σ_{sys} that is introduced into the calibrated standard magnitudes of science targets due to the errors in the fitted values of the coefficients Z, k_j and a. We identify the following observational parameters that we may consider optimising for our standard star observations:

---

[2]Note that the ith instrumental magnitude measurement m_i belongs to the $p(i)$th standard star and the $j(i)$th observational grouping, where the adopted notation for p and j reflects the fact that both of the indices p and j are functions of the index i. However, in the rest of this report, we devolve to using the notation p and j for $p(i)$ and $j(i)$, respectively, in order to avoid confusion in our subscript notation.

[3]In fact, when a colour term is involved, photometric calibration is more complicated in that it requires observations in two filters and the solution of simultaneous equations.

- The number of standard stars observed in each standard star image.

- The S/N of the standard star observations.

- The range of airmass covered during each night of standard star observations.

- The range in colour of the standard stars that are observed.

- The number of standard star images that are obtained during each night of standard star observations.

- The number of photometric nights for which standard star observations are obtained and modelled.

Optimal constraints on the model parameters in Equation 1 may be obtained by maximising all of these observational parameters. However, there are many observational constraints that limit the amount and quality of the standard star data that we may obtain (e.g. a standard star field has a finite number of standard stars and is only visible for a certain period of the year, the more standard star observations that we perform reduces the amount of scientific integration time available, etc.).

Assessing the impact of each observational parameter listed above on the achieved precision in the calibration coefficients Z, k_j and a, and on the systematic error σ_{sys} introduced into the calibrated standard magnitudes, when fitting Equation 1, is not an easy problem to solve. We also want our chosen method of analysis of this problem to reflect as closely as possible the real distribution of our observations, both in terms of the stars observed and the S/N achieved. Hence we have opted to perform simulations of the standard star observations to characterise the impact of a chosen observing strategy, and to inform us of which strategy we should adopt in order to minimise our use of scientific integration time for standard star observations while satisfying the operational contraints we would like to achieve on the uncertainties in Z, k_j and a, and consequently on the value of σ_{sys}.

4.2 Defining The Photometric Noise Model

For our simulations, we intend to use the information from the reductions of our *real* observations of the standard star fields in order to provide the closest simulation conditions to those that will occur in our real standard star observing campaign. For each standard star image, the FORS2 pipeline provides a table of information on the standard stars that were observed. Our intention is to use this table to define the set of standard stars that are observed in a typical standard star image along with the uncertainty on each standard star instrumental magnitude measurement and the range in colour of the observed standard stars. This approach allows us to avoid the need to invent a model for these observational parameters.

As described in Section 3.5, we have fixed the standard star identification problem in the FORS2 pipeline. However, for the purpose of the simulations we wish to run, we require a set of standard star images to have been correctly processed by the FORS2 pipeline to yield photometric tables. To this end, we have reprocessed the standard star imaging data for the two months from 01/12/2009 to 31/01/2010 ($\sim$60 images per filter) using a corrected version of the FORS2 pipeline (version 4.9.2). Although these observations do not necessarily match with the modified set of standard star fields that we wish to observe in the future (see later in Section 5.3), they do provide a *conservative* baseline for what we can achieve with our standard star observations because our updated choice of standard star fields attempts to maximise the number of standard stars observed, their S/N and their colour range.

The simulations that we intend to run are Monte Carlo simulations where we use the calculated uncertainties on the standard star instrumental magnitudes reported by the FORS2 pipeline to generate random values of $(m_i - M_p)$ for each standard star observation. Therefore, in order for our simulations to be meaningful, the instrumental magnitude uncertainties should be reliable and representative of the real scatter in the measurements.

In the upper plot panels of Figures 4 & 5, we show examples of plots of $(m_i - M_p)$ versus catalogue standard magnitude M_p, where each plot corresponds to a single standard star image, and where the mean value $\langle m_i - M_p \rangle$ has been subtracted from the individual $(m_i - M_p)$ values. The deviations of the values of $[(m_i - M_p) - \langle m_i - M_p \rangle]$ from zero are due to various contributions. Since the terms Z and $k_j X_i$ in Equation 1 take the same values for each star in a single image (i.e. a single image has a constant zero point and total extinction), it is only the colour term $a(M_p - M_p')$ that contributes to the deviations, and this contribution is expected to be negligible (<0.01 mag) for typical values of $|a| \approx 0.01$. Therefore proper correction for the colour term in the plots in Figures 4 & 5 is not necessary.
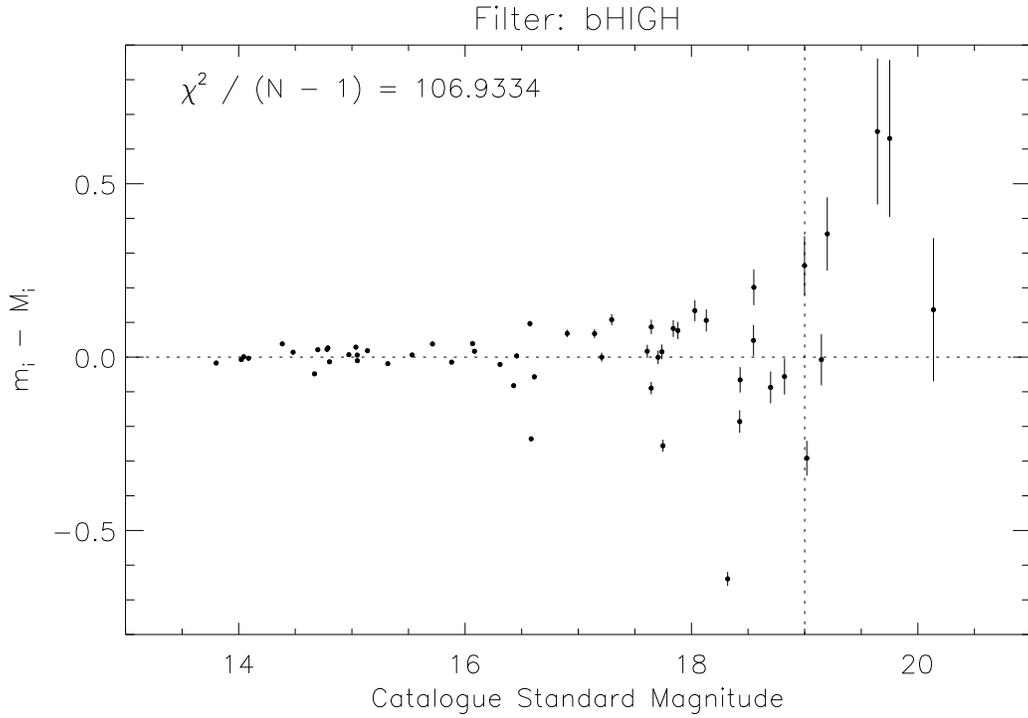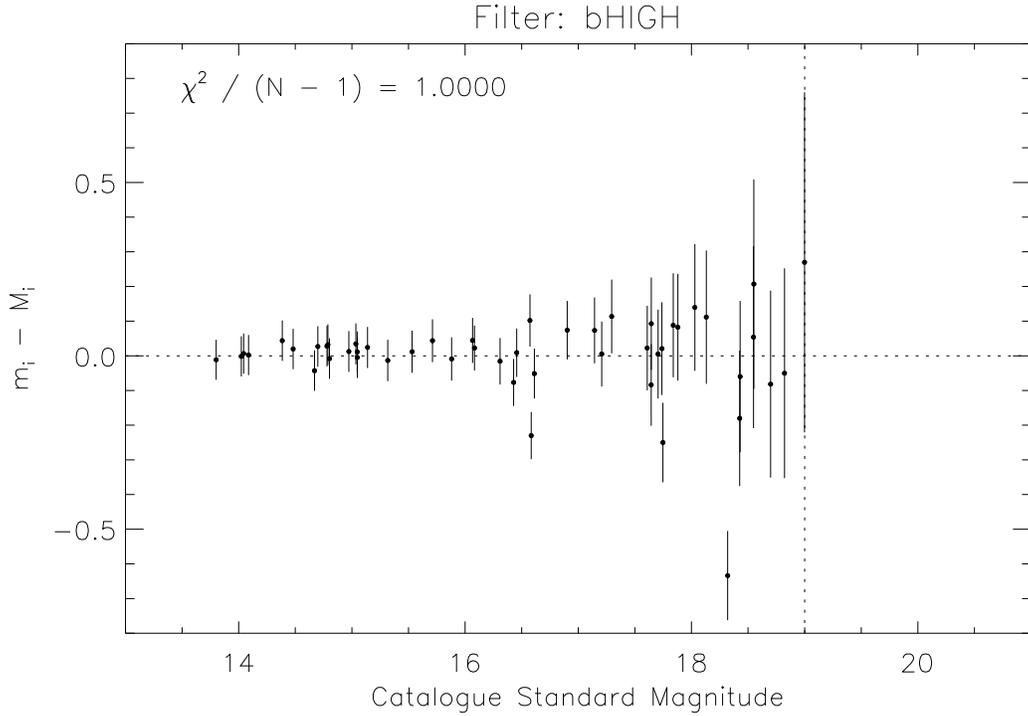
Figure 4: Plots of $(m_i - M_p)$ versus catalogue standard magnitude M_p where the mean value $\langle m_i - M_p \rangle$ has been subtracted from the individual $(m_i - M_p)$ values. The reduced chi squared around the mean value is reported in the top left corner of each plot. The vertical dotted line represents the magnitude cut-off for the B filter (see text). **Top panel:** The plot corresponds to a single standard star image. The uncertainties plotted on each data point are those reported by the FORS2 pipeline (version 4.9.2). **Bottom panel:** The same as the top panel after culling photometric data points below the magnitude cut-off, adding a systematic uncertainty of 0.01 mag in quadrature to the instrumental magnitude uncertainties, and then increasing the uncertainties by a factor of $\sim$5.74 to force a reduced chi squared of exactly 1.

17

Filter: bHIGH

$\chi^2 / (N - 1) = 7.5138$

Filter: bHIGH

$\chi^2 / (N - 1) = 1.0000$
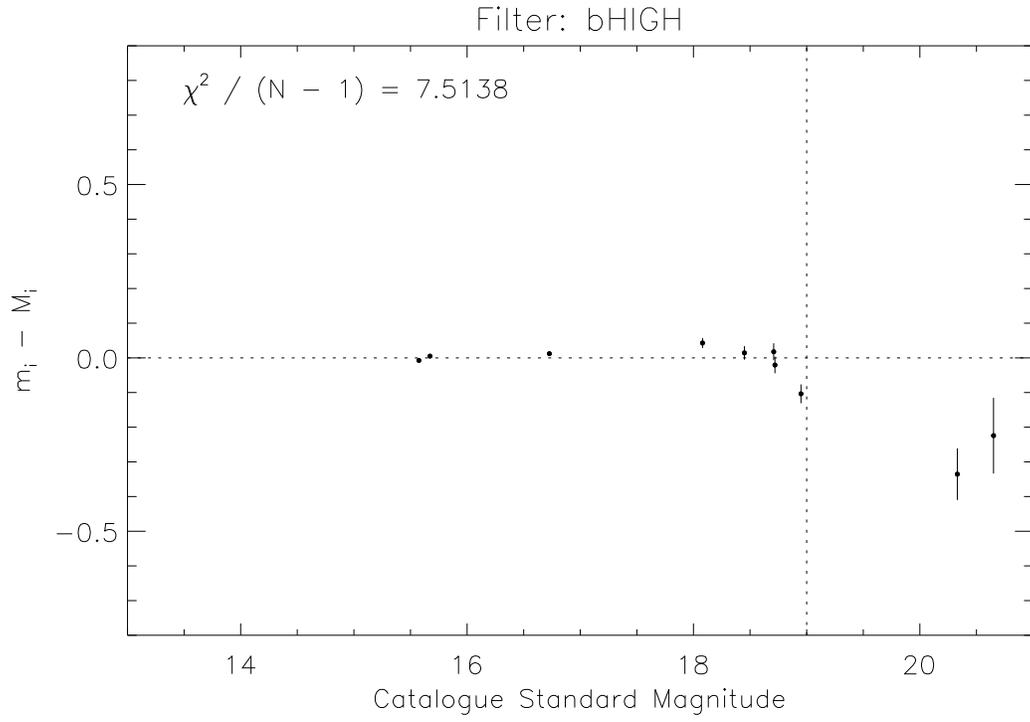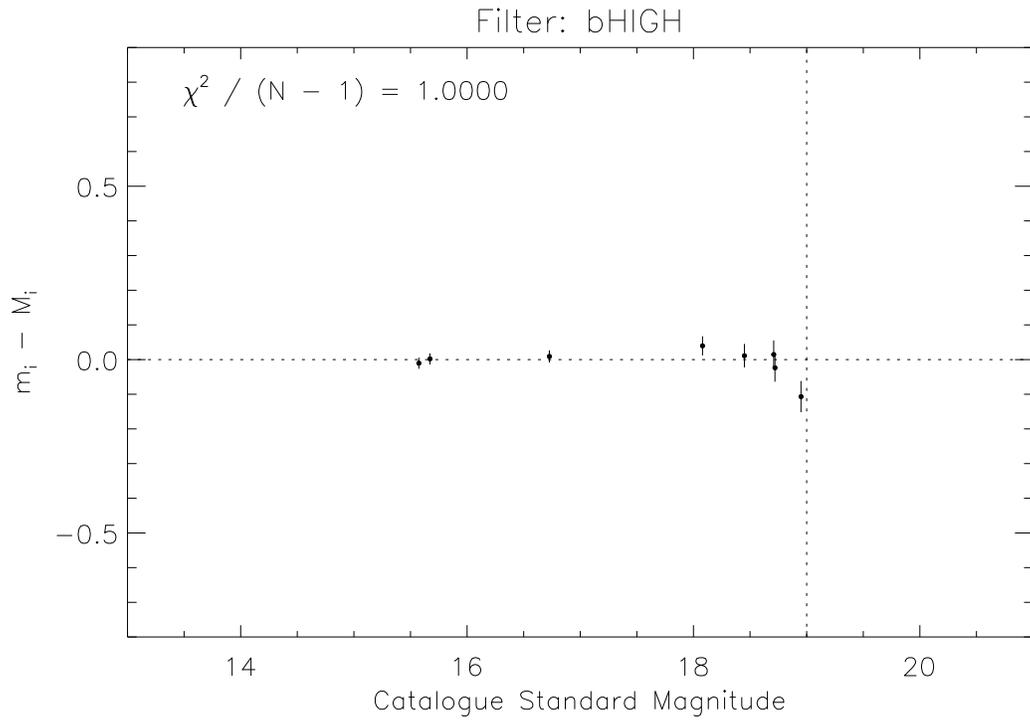
Figure 5: Same as Figure 4 for a different standard star image. In the bottom panel, photometric data points below the magnitude cut-off were culled, a systematic uncertainty of 0.01 mag was added in quadrature to the instrumental magnitude uncertainties, and then the uncertainties were increased by a factor of ∼1.56 to force a reduced chi squared of exactly 1.

Other contributions to the observed deviations come from random noise (readout noise and photon noise) mixed with unmodelled systematic errors (e.g. flat field errors, sky subtraction errors, differing spectral energy distributions for each star, systematic errors in the catalogue magnitudes, etc.). Inspection of the reduced chi squared in both cases indicates that the instrumental magnitude uncertainties are heavily underestimated ($\sim$0.001 mag for the bright stars) and that the systematic errors are dominant. In fact, in Figure 4(a), it is clear that the scatter in the bright star magnitude measurements is underestimated, and in Figure 5(a), errors in the sky estimation have caused a systematic error typical of aperture photometry for the fainter stars. We conclude that we cannot simply adopt the pipeline reported magnitude measurement uncertainties as a basis for the photometric measurement noise in our simulations.

To address the inconsistency between the pipeline reported instrumental magnitude uncertainties and the observed scatter in the data, we have adopted the following approach to reconcile the noise model with the data:

1. We apply a magnitude cut-off to the standard star photometric data so as to ignore standard stars with catalogue magnitudes fainter than 19.0, 18.5, 17.8 and 17.0 mag in the B, V, R and I bandpasses, respectively. This approach protects against systematic photometric errors for the fainter stars when sky subtraction errors may become dominant.

2. We then recalculate the mean value $\langle m_i - M_p \rangle$ for the subset of standard stars brighter than the magnitude cut-off limit and rederive the reduced chi squared. If the reduced chi squared is now less than or equal to 1, then we have finished. Otherwise, we proceed to add a constant uncertainty of 0.01 mag in quadrature to the uncertainties on the instrumental magnitude measurements. This quantity represents a fundamental limit to the accuracy of absolute photometry that may be achieved without modelling the full photometric system in exquisite detail (which is usually not possible or feasible). It also qualitatively matches the scatter in the photometry of the brighter stars in a reasonable proportion of the images that have been reduced.

3. Again, we recalculate the mean value $\langle m_i - M_p \rangle$ for the subset of standard stars brighter than the magnitude cut-off limit with the adjusted photometric uncertainties and rederive the reduced chi squared. If the reduced chi squared is now less than or equal to 1, then we have finished. Otherwise, we further scale the instrumental magnitude uncertainties by the square root of the reduced chi squared, which forces the reduced chi squared of a new calculation of the mean value $\langle m_i - M_p \rangle$ to equal exactly 1.

In both of the cases illustrated in Figures 4 & 5, it was necessary to apply all three of the above steps, and the uncertainty adjustment factors for the instrumental magnitude measurements in the last step are $\sim$5.74 and $\sim$1.56 for Figure 4(b) and Figure 5(b), respectively.

The above procedure was applied to the photometric tables produced from the reprocessing of the standard star images from 01/12/2009 to 31/01/2010 to prepare the input for our standard star observation simulations.

4.3 Generating The Simulation Data

As described at the beginning of Section 4.2, by using the information from real FORS2 observations of standard star fields in our simulations, we manage to fix various observational parameters to values directly relevant to FORS2 observations, therefore avoiding the need to construct an appropriate model for these parameters. The information we extract from the FORS2 pipeline photometric tables defines the number of stars observed in each standard star image, the S/N of each standard star observation (from the measured instrumental magnitude uncertainties modified as described at the end of Section 4.2), and the colours of the observed standard stars. Since we will be optimising these parameters in the future by specifying the best standard star fields to observe during each night of the year in the new calibration plan (see Section 5.3), our use of the relevant information from real FORS2 standard star observations serves to provide a conservative approximation for these parameters for the purpose of the simulations.

The remaining observational parameters which are not fixed in this way relate to how often standard star images are taken and at which airmasses, and the number of photometric nights used in the modelling of the data. These are the observational parameters that we have most control over in the FORS2 calibration plan. Our simulations are therefore designed to assess the effect of these remaining observational parameters on the accuracy of our photometric monitoring and calibrations.

We therefore primarily parameterise our simulations by the number of photometric nights N of observations of standard stars that are to be modelled using the photometric model described by Equation 1. We then consider the

effect of the number of standard star images observed per night and the achieved airmass range by specifying the following different observing strategies:

1. One standard star image is taken per night at airmass $X = 1.1$ for the N nights of observation, and the data from a single extra "photometric campaign" night are added where five standard star images are taken at airmasses of $X = 1.2, 1.4, 1.6, 1.8$ and 2.0. Without adding the photometric campaign night, it would be impossible to simultaneously solve for the photometric zero point and the nightly atmospheric extinction coefficients using these data.

2. Two standard star images are taken per night at airmasses of $X = 1.1$ and 1.4 for the N nights of observation.

3. Two standard star images are taken per night at airmasses of $X = 1.1$ and 1.4 for the N nights of observation, and the data from a single extra "photometric campaign" night are added where five standard star images are taken at airmasses of $X = 1.2, 1.4, 1.6, 1.8$ and 2.0.

4. Two standard star images are taken per night at airmasses of $X = 1.1$ and 1.8 for the N nights of observation.

5. Two standard star images are taken per night at airmasses of $X = 1.1$ and 1.8 for the N nights of observation, and the data from a single extra "photometric campaign" night are added where five standard star images are taken at airmasses of $X = 1.2, 1.4, 1.6, 1.8$ and 2.0.

6. Three standard star images are taken per night at airmasses of $X = 1.1, 1.4$ and 1.8 for the N nights of observation.

7. Three standard star images are taken per night at airmasses of $X = 1.1, 1.4$ and 1.8 for the N nights of observation, and the data from a single extra "photometric campaign" night are added where five standard star images are taken at airmasses of $X = 1.2, 1.4, 1.6, 1.8$ and 2.0.

We note that there are only ∼60 standard star images per filter that have been reprocessed with the corrected FORS2 pipeline, and therefore we are limited to a maximum value for N of ∼20 nights when considering simulations of three standard star images per night. Hence we limit our simulations to the range $2 < N < 20$.

In defining the simulations, it is also necessary to adopt some typical (but arbitrary) values for the parameters Z, k_j and a to which we may compare the values we derive from our analysis of the simulation data. We adopt $Z = -28.0$ mag, $k_j = 0.1$ mag/airmass for each night j, and $a = 0.05$.

For each filter, for each value of N, and for each observing strategy described above, we perform 10^6 simulations, where we generate and analyse the data for each simulation as follows:

1. From the ∼60 photometric tables for detector 1 corresponding to the standard star images that are available, we select the correct number of tables in time-order so as to cover the required number of images specified by the simulation (e.g. if $N = 5$ and two standard star images are observed per night along with a photometric campaign night, then we select the first 15 photometric tables for detector 1), and we assign an appropriate airmass to each table.

2. For each standard star entry in each selected photometric table, we generate a random value of $(m_i - M_p)$ from a Gaussian distribution with zero mean and standard deviation equal to the photometric uncertainty for the standard star entry. We then add to this value the standard magnitude M_p, the zero point Z, the total extinction $k_j X_i$ and the colour term $a(M_p - M'_p)$ using our adopted values of Z, k_j and a, and using the value of X_i specific to the photometric table and the values of M_p and $(M_p - M'_p)$ specific to the standard star. The final simulated value is stored as the instrumental magnitude measurement for the corresponding standard star in the corresponding photometric table. Note that by adopting a single value for k_j for each night, we are assuming that each night is photometric (i.e. has a stable extinction coefficient).

3. We proceed to fit the photometric model from Equation 1 relevant to the current simulation to the randomly generated instrumental magnitudes stored in the selected photometric tables, and we save the fitted values for Z, k_j and a.

4. Considering a reasonable airmass range of 1.0 to 1.8 and $V - R$ colour range of 0.3 to 1.4 mag for a typical science observation, we calculate the maximum possible systematic error σ_{sys} introduced when calibrating a science observation with the fitted values of Z, k_j and a as opposed to making the same calibration with the adopted simulation input values of Z, k_j and a. Note that the maximum systematic calibration error σ_{sys} is calculated not just over the assumed ranges of airmass and colour, but also over the nights of observation, therefore taking into account the different fitted values of k_j per night.

4.4   Simulation Results And Discussion

For each filter, for each number of photometric nights N of observations, and for each observing strategy described in Section 4.3, we have 10^6 fitted values of each of the photometric model parameters Z, k_j and a. In Figure 6, for each filter we plot the standard deviation (over the 10^6 simulations) in the derived values of the photometric zero point Z as a function of N. Different curves are shown for each observing strategy as described in the plot caption. These plots illustrate the precision to which we may monitor the photometric zero point as a function of the observational parameters of our simulations and based on real FORS2 standard star data.

From Figure 6, it can be seen that the zero point precision improves with N only if at least two standard star images are taken per night, and that ∼18 photometric nights with an airmass range of ∼0.7 should be included in the photometric modelling in order to obtain a monitoring precision of ∼1% across all filters. We may further conclude that the inclusion of observations at an intermediate airmass, or the inclusion of data from a photometric campaign night, provide little improvement in the monitoring precision for Z, as illustrated by the small differences between the lower solid red curve, the lower dashed red curve, and the black curves (solid and dashed).

We note that the nightly extinction coefficients k_j suffer from a systematic error (which is different for each simulation), in addition to a random error, relative to the input value of 0.1 mag/airmass (i.e. the mean value $< k_j >$ systematically differs from 0.1 mag/airmass for each simulation). This is due to the random error in the zero point systematically affecting the measured extinction coefficient for each nightly grouping of standard star images. We also note that this systematic error is substantially larger (by factors of ∼2-5) than the observed scatter in the k_j values derived for a single simulation. Hence we calculate the mean extinction coefficient $< k_j >$ over the nights of observation for each simulation, and in Figure 7, for each filter we plot the standard deviation (over the 10^6 simulations) in $< k_j >$ as a function of N and the different observing strategies in order to assess the impact of these parameters on the (dominant) induced systematic error in the extinction coefficients.

The plots in Figure 7 indicate that if we adopt the observing/modelling strategy of ∼18 photometric nights with two standard star images taken over an airmass range of 0.7 necessary for a ∼1% precision in the monitoring of the photometric zero point, then we will automatically achieve a better than ∼10% precision in the monitoring of the nightly extinction coefficient k_j in each filter.

In Figure 8, for each filter we plot the standard deviation (over the 10^6 simulations) in the derived values of the colour term coefficient a as a function of N and the different observing strategies. We note that increasing N improves the precision to which we can monitor a for each observing strategy and that changing the airmass range (from 0.3 to 0.7) has no effect on the monitoring precision (as can be seen by the coincidence of both solid red curves and both dashed red curves in each plot). We also note that increasing the number of standard star images observed per night, and the inclusion of the data from a photometric campaign night, may substantially improve the precision to which we can monitor a. However, the precision to which we can monitor a is not a driving constraint for our observational strategy, and adopting the observing/modelling strategy of ∼18 photometric nights with two standard star images taken over an airmass range of 0.7 necessary for a ∼1% precision in the monitoring of the photometric zero point results in an ability to monitor a to a precision of ∼20-30% in each filter.

Finally, in Figure 9, for each filter we plot the mean (over the 10^6 simulations) of the maximum possible systematic error σ_{sys} that may be introduced into the calibrated standard magnitude of a science object by using the fitted photometric calibration coefficients Z, k_j and a as a function of N and the different observing strategies. The left-hand column of plots corresponds to the maximum possible systematic error calculated for nights with regular standard star observations of 1,2 or 3 standard star images taken per night, and the right-hand column of plots corresponds to the maximum possible systematic error calculated for the photometric campaign night.

Again, we see that the photometric calibration accuracy improves with N only if at least two standard star images are taken per night. We also see that increased numbers of standard star observations per night and an increased airmass
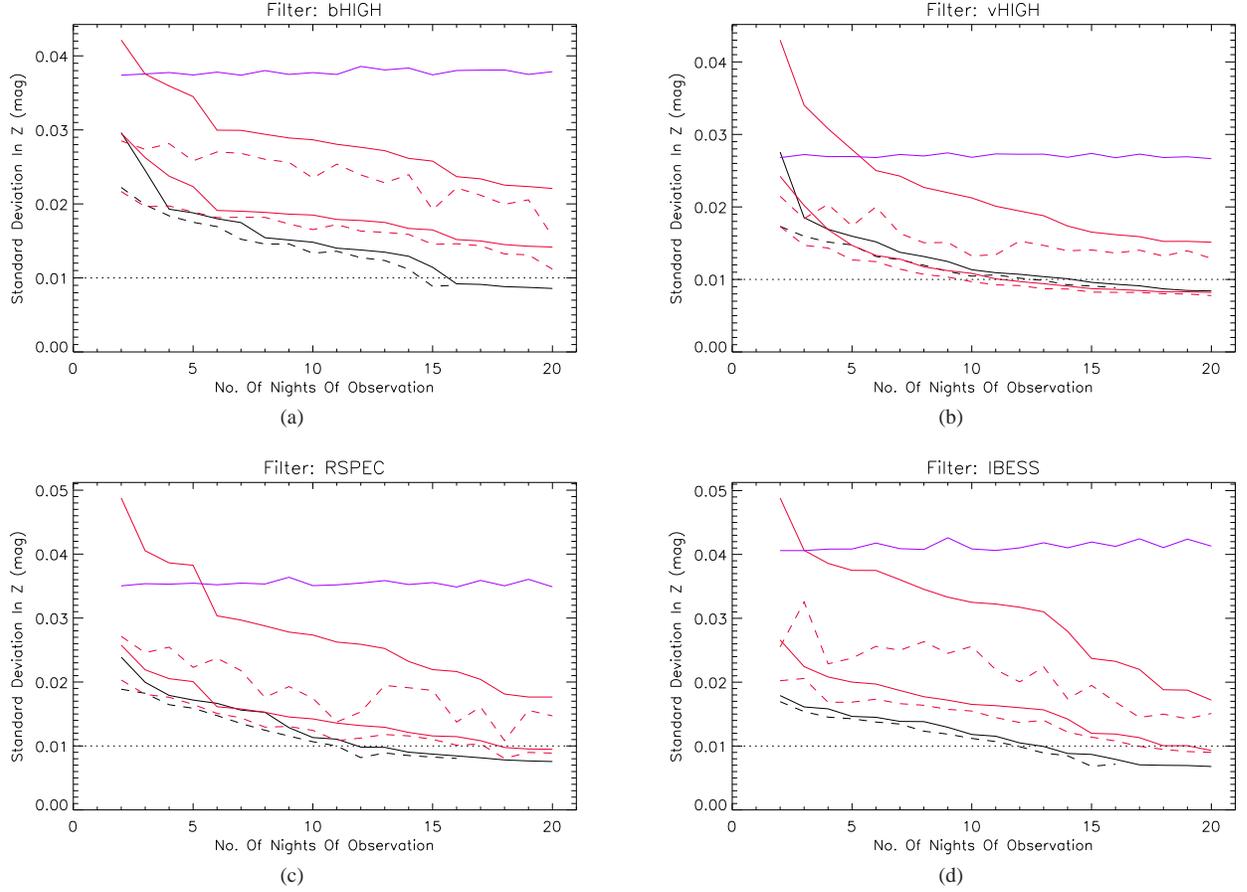
Figure 6: Plots of the standard deviation (over the 10^6 simulations) of the measured zero point Z (mag) as a function of the number of photometric nights of standard star observations. Each plot corresponds to a different filter (reported in the title). The blue curve corresponds to one standard star image taken per night at an airmass of $X = 1.1$ with the addition of an extra photometric campaign night of five standard star images taken at airmasses of $X = 1.2, 1.4, 1.6,$ 1.8 and 2.0. The solid red curves correspond to two standard star images taken per night at airmasses of $X = 1.1$ and 1.4 for the upper curve, and at airmasses of $X = 1.1$ and 1.8 for the lower curve. The dashed red curves also correspond to two standard star images taken per night at airmasses of $X = 1.1$ and 1.4 for the upper curve, and at airmasses of $X = 1.1$ and 1.8 for the lower curve, but with the addition of an extra photometric campaign night (same as for the blue curve). The solid black curve corresponds to three standard star images taken per night at airmasses of $X = 1.1, 1.4$ and 1.8, and the dashed black curve corresponds to three standard star images taken per night at airmasses of $X = 1.1, 1.4$ and 1.8 with the addition of an extra photometric campaign night (same as for the blue curve). The horizontal dotted line indicates the desired monitoring precision for the photometric zero point.
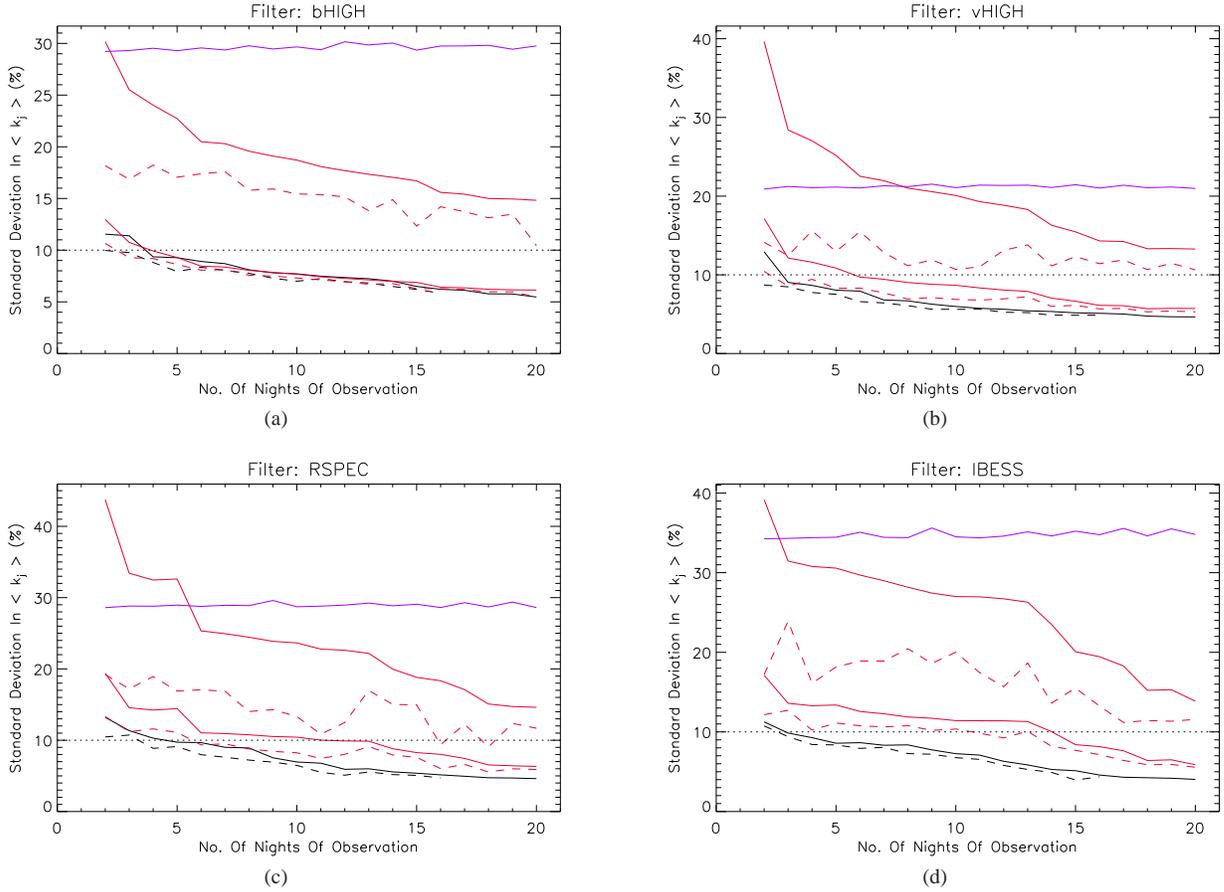
Figure 7: Plots of the standard deviation (over the 10^6 simulations) of the measured mean extinction coefficient $< k_j >$ over the nights of observation as a function of the number of photometric nights of standard star observations. Note that the standard deviations have been converted to a percentage of the adopted extinction coefficient used as input to the simulations. Each plot corresponds to a different filter (reported in the title). Curve descriptions are the same as for Figure 6. The horizontal dotted line indicates the desired monitoring precision for the atmospheric extinction coefficients.
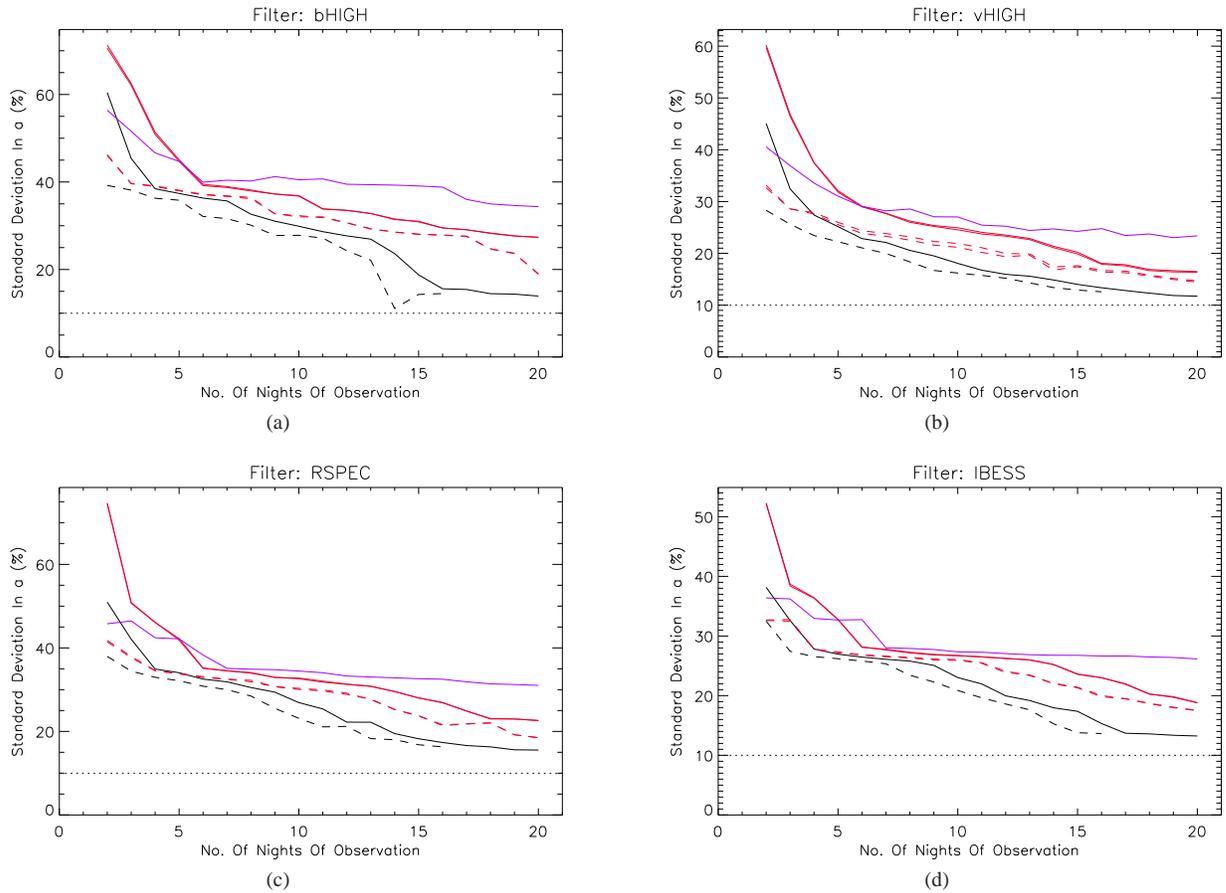
Figure 8: Plots of the standard deviation (over the 10^6 simulations) of the measured colour term coefficient a as a function of the number of photometric nights of standard star observations. Note that the standard deviations have been converted to a percentage of the adopted colour term coefficient used as input to the simulations. Each plot corresponds to a different filter (reported in the title). Curve descriptions are the same as for Figure 6. The horizontal dotted line indicates the desired monitoring precision for the colour term coefficient.
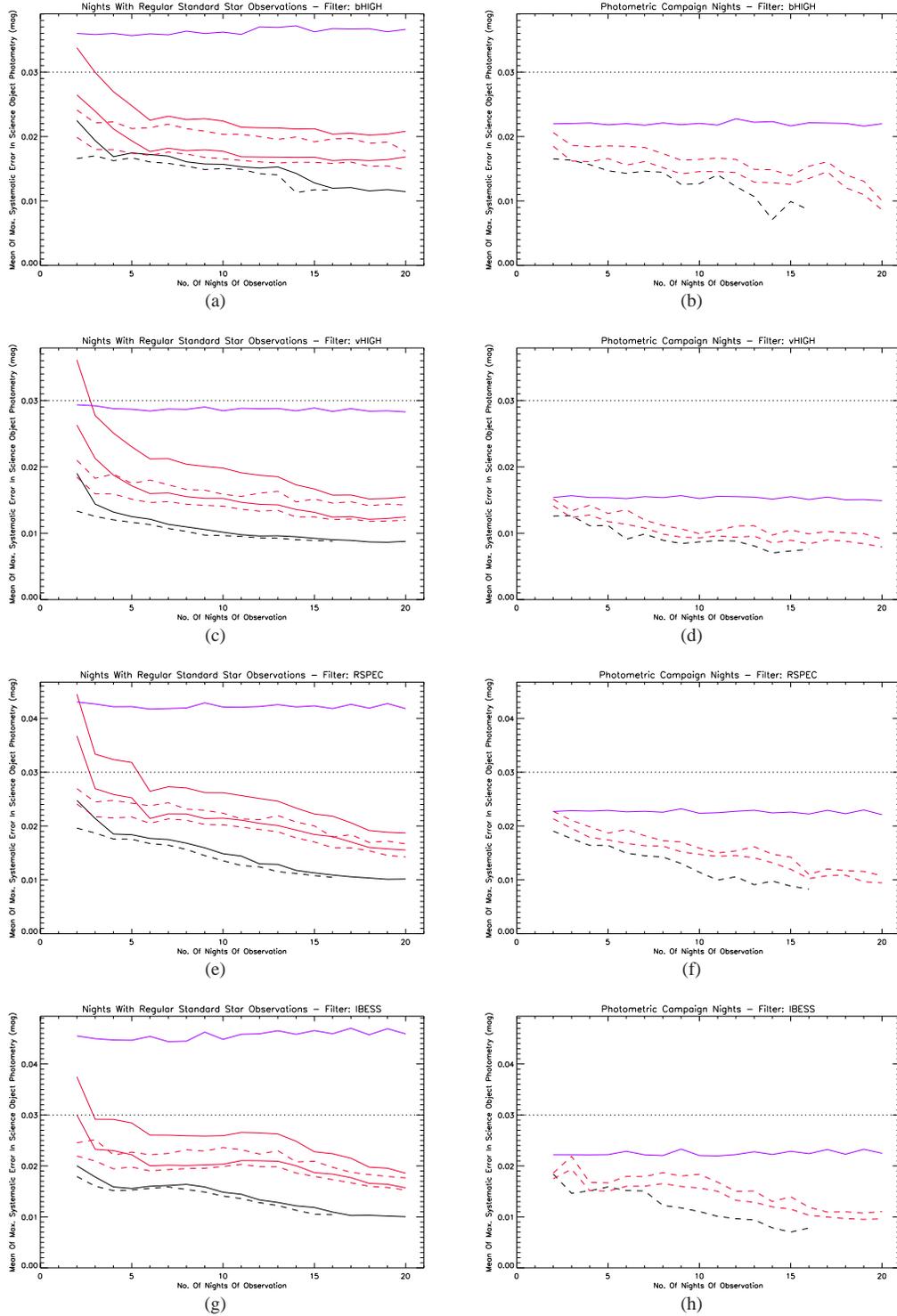
Figure 9: Plots of the mean (over the 10^6 simulations) of the maximum possible systematic error σ_{sys} (mag) that may be introduced into the calibrated standard magnitude of a science object by using the fitted photometric calibration coefficients Z, k_j and a versus the number of photometric nights of standard star observations. Each plot corresponds to a different filter (reported in the title). The left-hand column of plots corresponds to the maximum possible systematic error calculated for the nights with regular standard star observations of 1, 2 or 3 standard star images taken per night. The right-hand column of plots corresponds to the maximum possible systematic error calculated for the photometric campaign night where five standard star images are taken at airmasses of $X = 1.2$, 1.4, 1.6, 1.8 and 2.0. The horizontal dotted line indicates the desired absolute photometric accuracy that we wish to provide the user the ability to achieve with the photometric calibration of FORS2 observations (given sufficient science object S/N).

25

range of observations both work to improve the achievable photometric calibration accuracy. Furthermore, the impact of a photometric campaign night of standard star observations on the achievable photometric accuracy for any night (including the photometric campaign night) is relatively small (except when only one standard star image is taken per night, in which case the achievable photometric accuracy on the photometric campaign night is approximately twice as good as on any other night). However, the plots in Figure 9 clearly show that in order to achieve the FAP aim of an absolute photometric accuracy of 3%, an observing strategy with at least two standard star images taken per night and including at least 4 photometric nights in the modelling is sufficient.

4.5 Conclusions

The results of the simulations are very similar between filters, and so the conclusions we make about the recommended standard star observing strategy for the FORS2 instrument apply to all of the broadband filters B, V, R and I:

1. To achieve a $\sim$1% monitoring precision for the photometric zero point, important for assessing changes in the detector+instrument+telescope sensitivity, one should obtain two standard star images per night at airmasses of $X \approx 1.1$ and 1.8, ensuring a range in airmass of $\sim$0.6 to 0.7, and at least 18 photometric nights should be included in the photometric modelling of the data.

2. It is important to note that the results from the simulations performed in this Section depend on the assumption that the extinction coefficient is stable for the time period over which the standard star images are observed during any one night. Therefore, in order to minimise the probability of violating this assumption, it is desirable to obtain the minimum two standard star images for the night that cover the required airmass range of $\sim$0.6 to 0.7 as close together in time as possible.

3. Observations coupled with modelling satisfying the constraints described in (1) & (2) will enable the monitoring of the atmospheric extinction coefficient to a precision of $\sim$6-8%. Similarly, the colour term coefficient, again linked to the instrumental optical properties, may be monitored with a $\sim$20-30% precision.

4. The FAP project goal of providing the user with the ability to reach an absolute photometric accuracy of 3% with the FORS2 instrument may be achieved by following the constraints described in (1) & (2), which in fact lead to the ability to reach absolute photometric accuracies of 1.4-1.8%.

5. Once two standard star images at airmasses of $X \approx 1.1$ and 1.8 have been obtained, further images taken at intermediate airmasses have little impact on the precision of the monitoring of the photometric zero point and the extinction coefficient for the night in question. However, such extra observations serve to verify that the fitted extinction coefficient for the night is stable, potentially allowing for the classification of the night as photometric (stable extinction coefficient) or non-photometric (variable extinction coefficient). Further images may also provide some improvements in the achievable absolute photometric calibration accuracy for science objects (but with diminishing returns for the time invested).

We note that previous FAP documents (Freudling et al. 2006; Freudling et al. 2007) have recommended that three standard star observations should be taken during a photometric night over a range of airmasses in order to achieve a precision of $\sim$1% in the determined photometric zero point. However, our detailed investigation of the observing (and modelling) strategy required to achieve this goal in parallel with the aim of enabling an absolute photometric accuracy of 3% for FORS2 science observations indicates that this constraint may be relaxed into taking two standard star observations per night over a large enough range in airmass ($\sim$0.6-0.7) so long as at least 18 photometric nights with similar data are included in the photometric modelling.

5 FORS2 Calibration Plans

In this Section, we use the conclusions from Section 4.5 as a basis for designing a new FORS2 calibration plan, which should enable us to achieve the monitoring and calibration goals stated in Section 4.1.

5.1 The Current Calibration Plan Is Not Being Followed

Using data from the Science Archive Facility, we extracted information on the observational epochs and airmasses of the standard star images that were obtained with FORS2 during the period 01/01/2011 to 10/04/2011. In Figure 10, we plot the separation in time of the standard star images taken during a night as a function of observation date, and in Figure 11, we plot the airmass distribution of the standard star images as a function of observation date. In both plots, red and green data points represent standard star images taken on nominally non-photometric and photometric nights, respectively, where this classification is made by the QC scientist based on LOSSAM[4] data (and in ambiguous situations by consulting the night report in addition).

The FORS2 photometric calibration plan that is described in the FORS2 manual (Saviane 2010) is out of date, and for convenience we reproduce in Appendix B the instructions for the current (July 2011) calibration plan at Paranal. It specifies the requirement per broadband filter for a nightly observation of a standard star field and a further observation of a standard star field at high airmass (>1.6) for those nights that are considered as photometric. From Figures 10 & 11, one can see that this calibration plan has not been followed, with many pairs of standard star images not achieving the high airmass constraint, and with a reasonable proportion of photometric nights failing to have at least two standard star observations. The consequence of this is that the standard star photometric data that we are gathering are not sufficient to be able to satisfy our monitoring goal of $\sim$1% precision for the photometric zero point or our goal of enabling 3% absolute photometric accuracy. This demonstrates the importance of monitoring the implementation of the calibration plan more closely in the future.

5.2 Proposal For A New Calibration Plan

We propose the following new calibration plan, based on the conclusions derived from the results of the simulations presented in Section 4:

1. Whenever FORS2 comes on for the first time during the night and is expected to be observing for more than $\sim$4 hours, a standard star field at low airmass should be observed for each broadband filter (B, V, R and I), unless the sky has thin/thick clouds. If the extinction coefficients derived from this observation serve to classify the night as photometric, then another standard star field should be observed immediately afterwards at high airmass, such that the difference in airmass between the observations is greater than or equal to 0.7. Both fields should be chosen following the recommended Stetson standard star fields listed for different times of the year in Section 5.3.

2. If a night is flagged as photometric and science data requiring photometric conditions are to be obtained, then further observations of standard stars should be carried out during the night in order to monitor the continued stability of the conditions. These observations should be carried out with the same filter(s) as the science observations. Observing one standard star field in the middle of the night and another at the end of the night is sufficient. The airmasses of these two fields should be chosen to further sample the previously observed airmass range (e.g. if observations at the beginning of the night were performed at airmasses of 1.1 and 1.9, then the observations in the middle of the night and at the end of the night could be obtained at airmasses of $\sim$1.3 and $\sim$1.6).

3. Standard star fields should be selected in order to maximise the number of standard stars observed and the range in colour (ideally with $\Delta(B-V)$ and $\Delta(V-R)$ of at least $\sim$0.8 mag). The standard star fields listed in Section 5.3 have already been prioritised according to this recommendation.

4. Each observation of the same standard star field should be taken using a different offset and rotation so that over the course of a few months the full set of offsets and rotations specified in the relevant offset file is performed (see Table 1 & Appendix C). This strategy ensures that the standard star observations sample the full area of each detector and a full rotation, potentially enabling the calibration of systematic spatially-dependent photometric errors (i.e. static and rotating illumination corrections) in the science object photometry. The set of offsets and rotations to be observed depends on the standard star field in question, since they must be distributed so as

---

[4]see http://www.eso.org/gen-fac/pubs/astclim/paranal/asm/lossam/study.html and http://archive.eso.org/asm/ambient-server
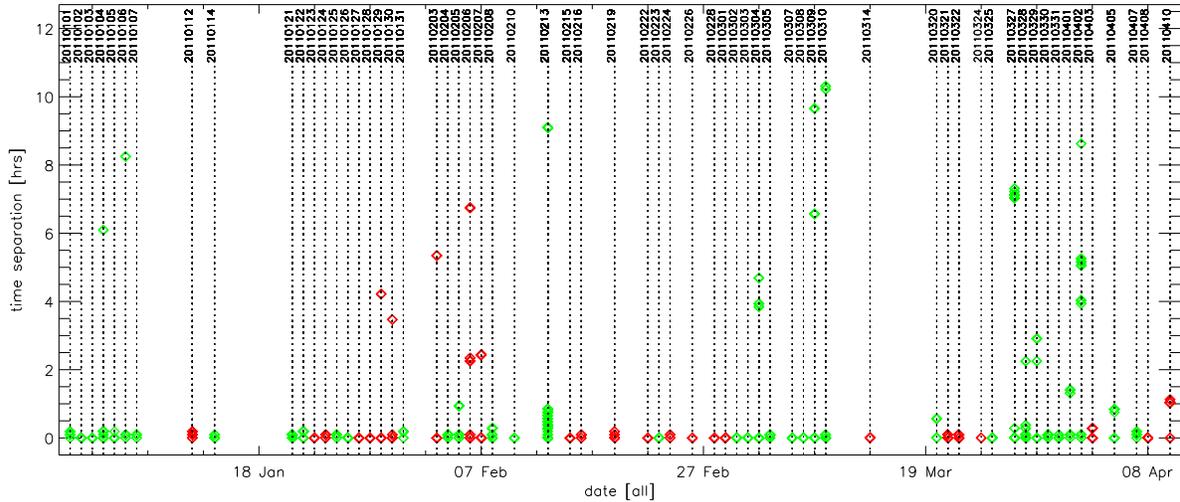
Figure 10: Plot of the separation in time of the standard star images taken during a night as a function of observation date for the period 01/01/2011 to 10/04/2011. Red and green data points represent standard star images taken on nominally non-photometric and photometric nights, respectively, as classified by the QC scientist.
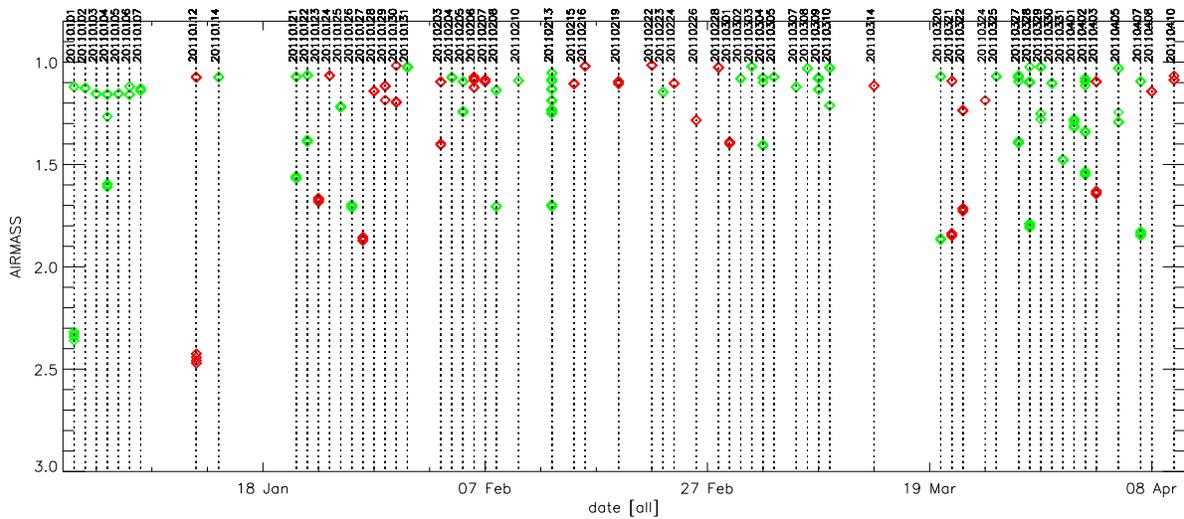
Figure 11: Plot of the airmass distribution of the standard star images as a function of observation date for the period 01/01/2011 to 10/04/2011. Red and green data points represent standard star images taken on nominally non-photometric and photometric nights, respectively, as classified by the QC scientist.

to avoid placing very bright stars on the detector and to ensure that a reasonable number of standard stars are present in the images.

5. Observations of standard star fields that are close to the Moon should be avoided since the scattered moonlight will reduce the S/N of the photometry and cause unwanted sky gradients in the images. The exact limit on the target-Moon distance should be decided by Paranal.

Table 1: The Stetson standard star fields.

Name	R.A. [hh:mm:ss]	DEC [±dd:mm:ss]	Nstars	$\Delta(B-V)$ [mag]	$\Delta(V-R)$ [mag]	Texp [sec]	Offsets File ID
(1)	(2)	(3)	(4)	(5)	(6)	(7)	(8)
T-Phe	00:30:06.3	-46:28:08.6	14	1.00	0.71	B,V,R=3sec; I=1sec	0
L92	00:55:09.7	+00:42:49.9	19	0.66	0.42	B,V,R=3sec; I=1sec	2
PG0231	02:33:40.9	+05:19:15.0	12	0.78	0.45	B,V,R=4sec; I=1.5sec	1
L95	03:53:38.7	+00:07:16.7	21	0.79	0.59	B,V,R=3sec; I=1sec	1
E3	06:43:13.6	-45:13:28.8	39	0.93	0.60	B,V,R=3sec; I=1sec	3
NGC2298	06:48:37.2	-35:58:34.6	126	1.23	0.88	B,V,R=3sec; I=1sec	2
L98	06:52:09.3	-00:19:00.3	165	1.38	1.05	B,V,R=3sec; I=1sec	1
Ru149	07:24:16.7	-00:32:20.1	207	1.21	0.86	B,V,R=3sec; I=1sec	1
Ru152	07:29:56.5	-02:05:42.1	63	0.91	0.54	B,V,R=3sec; I=1sec	1
NGC2420	07:38:28.3	+21:34:02.9	47	0.61	0.30	B,V,R=3sec; I=1sec	3
NGC2437	07:41:41.0	-14:50:45.8	65	1.17	0.80	B,V,R=3sec; I=1sec	1
NGC2818	09:16:22.9	-36:35:20.2	173	1.18	0.78	B,V,R=3sec; I=1sec	2
L101	09:56:53.0	-00:19:53.7	21	1.09	0.74	B,V,R=3sec; I=1sec	1
LeoI	10:08:55.1	+12:22:37.6	34	1.17	0.77	B,V,R=3sec; I=1sec	2
PG1047	10:50:05.3	-00:00:57.4	14	0.77	0.50	B,V,R=4sec; I=1.5sec	1
E5	12:05:13.3	-45:33:56.5	69	0.92	0.56	B,V,R=3sec; I=1sec	1
L104	12:42:17.2	-00:31:51.6	20	1.09	0.68	B,V,R=4sec; I=1.5sec	1
PG1323	13:25:45.0	-08:49:59.3	13	0.52	0.24	B,V,R=3sec; I=1sec	1
NGC5139$^{(*)}$	13:26:30.0	-47:10:23.0	100	1.12	0.60	B,V,R=3sec; I=1sec	1
IC4499$^{(*)}$	14:57:50.0	-82:12:00.0	41	0.45	0.27	B,V,R=3sec; I=1sec	2
PG1525	15:28:11.0	-07:14:34.2	21	1.05	0.68	B,V,R=4sec; I=1.5sec	1
L107	15:39:32.7	-00:12:32.0	25	0.91	0.61	B,V,R=3sec; I=1sec	1
NGC6121$^{(*)}$	16:24:10.0	-26:35:03.0	50	0.90	0.50	B,V,R=3sec; I=1sec	2
PG1633	16:35:12.1	+09:50:59.0	60	0.92	0.61	B,V,R=3sec; I=1sec	1
PG1657	16:59:35.5	+07:42:31.0	78	1.01	0.72	B,V,R=3sec; I=1sec	0
E7	17:27:20.0	-45:02:28.0	182	1.36	1.06	B,V,R=3sec; I=1sec	2
L110	18:42:46.1	+00:07:04.9	49	1.99	1.44	B,V,R=3sec; I=1sec	1
NGC6822$^{(*)}$	19:44:53.0	-14:37:50.0	67	1.29	0.87	B,V,R=3sec; I=1sec	2
NGC6940	20:34:32.0	+28:14:50.0	90	1.12	0.77	B,V,R=3sec; I=1sec	2
MarkA	20:43:39.6	-10:46:29.0	60	1.07	0.78	B,V,R=3sec; I=1sec	1
NGC7006	21:01:15.7	+16:11:26.7	19	0.43	0.30	B,V,R=3sec; I=1sec	2
PG2213	22:16:19.1	-00:21:14.1	22	0.88	0.64	B,V,R=3sec; I=1sec	1

Notes –

Col. 1: Name of the field, according to http://www2.cadc-ccda.hia-iha.nrc-cnrc.gc.ca/community/STETSON/standards/. Fields labeled with $^{(*)}$ were not observed within the FORS2 calibration plan from 01/01/2009 to 10/04/2011, and therefore they have not been fully assessed for suitability for use as FORS2 standard star fields.

Cols. 2-3: Celestial coordinates for the optimal pointing with FORS2 (to avoid too few stars or overcrowding etc.). Note that these coordinates may differ from those listed in the Stetson catalogue.

Col. 4: Estimate of the number of standard stars present in the FORS2 field with $S/N \geq 20$ on the basis of FORS2 archive images (corresponding to $B < 19$). For the fields never observed with FORS2 (marked with $^{(*)}$ in Col. 1), an estimate is made on the basis of the B catalogue magnitudes. Please note that this number refers to the total number of stars present over both detectors.

Cols.5-6: Spread in colour of the stars visible in the FORS2 field with $S/N \geq 20$.

Col. 7: Recommended exposure time.

Col. 8: ID number of the offset file to adopt: offsets_ID.dat (see Appendix C).

5.3 Recommended Stetson Standard Star Fields

In Table 1, we list the full set of Stetson standard star fields from the Stetson standard star catalogue with recommended pointings and exposure times relevant to the FORS2 instrument. This list of standard star fields has been used to create individual recommendations for specific standard star fields to be observed at different times of the year, based on primarily satisfying the airmass constraints in the proposed calibration plan, and then on optimising the number of standard stars that are observed along with the colour range that is achieved. For each period of approximately 15 days in a year, we list below the standard star fields that should be observed at the beginning, middle and end of the night. In case these fields cannot be observed for some reason (moon constraints etc.), a backup list of standard star fields is provided in order of priority.

More detailed information on the chosen Stetson standard star fields may be found at:
http://www.eso.org/~lcoccato/duties_web/fields/visibility.html

01 - 14 January
Beginning of the night: L95 ($z \sim 1.13$), L98 ($z \sim 2.03$)
Middle of the night: NGC2298
End of the night: NGC2298

Suitable fields in this period:

Name	R.A. [hh:mm:ss]	DEC [±dd:mm:ss]	Nstars	$\Delta(B-V)$ [mag]	$\Delta(V-R)$ [mag]
Ru149	07:24:16.7	-00:32:20.1	207	1.21	0.86
NGC2818	09:16:22.9	-36:35:20.2	173	1.18	0.78
L98	06:52:09.3	-00:19:00.3	165	1.38	1.05
NGC2298	06:48:37.2	-35:58:34.6	126	1.23	0.88
L101	09:56:53.0	-00:19:53.7	21	1.09	0.74
L95	03:53:38.7	+00:07:16.7	21	0.79	0.59

15 - 31 January
Beginning of the night: L95 ($z \sim 1.10$), Ru149 ($z \sim 1.76$)
Middle of the night: NGC2298
End of the night: LeoI

Suitable fields in this period:

Name	R.A. [hh:mm:ss]	DEC [±dd:mm:ss]	Nstars	$\Delta(B-V)$ [mag]	$\Delta(V-R)$ [mag]
Ru149	07:24:16.7	-00:32:20.1	207	1.21	0.86
NGC2818	09:16:22.9	-36:35:20.2	173	1.18	0.78
L98	06:52:09.3	-00:19:00.3	165	1.38	1.05
NGC2298	06:48:37.2	-35:58:34.6	126	1.23	0.88
LeoI	10:08:55.1	+12:22:37.6	34	1.17	0.77
L95	03:53:38.7	+00:07:16.7	21	0.79	0.59

01 - 13 February
Beginning of the night: NGC2298 ($z \sim 1.12$), NGC2818 ($z \sim 1.79$)
Middle of the night: NGC2818
End of the night: NGC2818

Suitable fields in this period:

Name	R.A. [hh:mm:ss]	DEC [±dd:mm:ss]	Nstars	$\Delta(B-V)$ [mag]	$\Delta(V-R)$ [mag]
Ru149	07:24:16.7	-00:32:20.1	207	1.21	0.86
E7	17:27:20.0	-45:02:28.0	182	1.36	1.06
N2818	09:16:22.9	-36:35:20.2	173	1.18	0.78
L98	06:52:09.3	-00:19:00.3	165	1.38	1.05
N2298	06:48:37.2	-35:58:34.6	126	1.23	0.88
N6940	20:34:32.0	+28:15:10.0	90	1.12	0.77
N2437	07:41:41.0	-14:50:45.8	65	1.17	0.80
MarkA	20:43:39.6	-10:46:29.0	60	1.07	0.78
E5	12:05:13.3	-45:33:56.5	69	0.92	0.56
LeoI	10:08:55.1	+12:22:37.6	34	1.17	0.77

14 - 29 February

Beginning of the night: NGC2298 ($z \sim 1.05$), NGC2420 ($z \sim 1.71$)
Middle of the night: Ru149
End of the night: E7

Suitable fields in this period:

Name	R.A. [hh:mm:ss]	DEC [±dd:mm:ss]	Nstars	$\Delta(B-V)$ [mag]	$\Delta(V-R)$ [mag]
Ru149	07:24:16.7	-00:32:20.1	207	1.21	0.86
E7	17:27:20.0	-45:02:28.0	182	1.36	1.06
N2818	09:16:22.9	-36:35:20.2	173	1.18	0.78
N2298	06:48:37.2	-35:58:34.6	126	1.23	0.88
N2437	07:41:41.0	-14:50:45.8	65	1.17	0.80
N6940	20:34:32.0	+28:15:10.0	90	1.12	0.77
MarkA	20:43:39.6	-10:46:29.0	60	1.07	0.78
E5	12:05:13.3	-45:33:56.5	69	0.92	0.56
LeoI	10:08:55.1	+12:22:37.6	34	1.17	0.77
N2420	07:38:28.3	+21:34:02.9	47	0.61	0.30

01 - 14 March

Beginning of the night: NGC2298 ($z \sim 1.02$), L101 ($z \sim 1.85$)
Middle of the night: NGC2437
End of the night: E7

Suitable fields in this period:

Name	R.A. [hh:mm:ss]	DEC [±dd:mm:ss]	Nstars	$\Delta(B-V)$ [mag]	$\Delta(V-R)$ [mag]
Ru149	07:24:16.7	-00:32:20.1	207	1.21	0.86
E7	17:27:20.0	-45:02:28.0	182	1.36	1.06
N2298	06:48:37.2	-35:58:34.6	126	1.23	0.88
NGC2437	07:41:41.0	-14:50:45.8	65	1.17	0.80
MarkA	20:43:39.6	-10:46:29.0	60	1.07	0.78
E5	12:05:13.3	-45:33:56.5	69	0.92	0.56
L101	09:56:53.0	-00:19:53.7	21	1.09	0.74

15 - 31 March

Beginning of the night: NGC2298 ($z \sim 1.02$), LeoI ($z \sim 1.91$)
Middle of the night: LeoI
End of the night: E7

Suitable fields in this period:

Name	R.A. [hh:mm:ss]	DEC [±dd:mm:ss]	Nstars	$\Delta(B-V)$ [mag]	$\Delta(V-R)$ [mag]
Ru149	07:24:16.7	-00:32:20.1	207	1.21	0.86
E7	17:27:20.0	-45:02:28.0	182	1.36	1.06
N2298	06:48:37.2	-35:58:34.6	126	1.23	0.88
L101	09:56:53.0	-00:19:53.7	21	1.09	0.74
LeoI	10:08:55.1	+12:22:37.6	34	1.17	0.77
E5	12:05:13.3	-45:33:56.5	69	0.92	0.56

01 - 14 April

Beginning of the night: NGC2437 ($z \sim 1.02$), E5 ($z \sim 1.71$)
Middle of the night: NGC2818
End of the night: MarkA

Suitable fields in this period:

Name	R.A. [hh:mm:ss]	DEC [±dd:mm:ss]	Nstars	$\Delta(B-V)$ [mag]	$\Delta(V-R)$ [mag]
E7	17:27:20.0	-45:02:28.0	182	1.36	1.06
N2818	09:16:22.9	-36:35:20.2	173	1.18	0.78
N2298	06:48:37.2	-35:58:34.6	126	1.23	0.88
PG1657	16:59:35.5	+07:42:31.0	78	1.01	0.72
N2437	07:41:41.0	-14:50:45.8	65	1.17	0.80
MarkA	20:43:39.6	-10:46:29.0	60	1.07	0.78
E5	12:05:13.3	-45:33:56.5	69	0.92	0.56

15 - 30 April

Beginning of the night: NGC2818 ($z \sim 1.04$), NGC5139 ($z \sim 2.06$)
Middle of the night: E7
End of the night: MarkA

Suitable fields in this period:

Name	R.A. [hh:mm:ss]	DEC [±dd:mm:ss]	Nstars	$\Delta(B-V)$ [mag]	$\Delta(V-R)$ [mag]
E7	17:27:20.0	-45:02:28.0	182	1.36	1.06
N2818	09:16:22.9	-36:35:20.2	173	1.18	0.78
PG1657	16:59:35.5	+07:42:31.0	78	1.01	0.72
NGC5139*	13:26:30.0	-47:10:23.0	100	1.12	0.60
MarkA	20:43:39.6	-10:46:29.0	60	1.07	0.78
LeoI	10:08:55.1	+12:22:37.6	34	1.17	0.77
N6940	20:34:32.0	+28:15:10.0	90	1.12	0.77

01 - 14 May

Beginning of the night: NGC2818 ($z \sim 1.02$), PG1323 ($z \sim 1.95$)
Middle of the night: E7
End of the night: E7

Suitable fields in this period:

Name	R.A. [hh:mm:ss]	DEC [±dd:mm:ss]	Nstars	$\Delta(B-V)$ [mag]	$\Delta(V-R)$ [mag]
Ru149	07:24:16.7	-00:32:20.1	207	1.21	0.86
E7	17:27:20.0	-45:02:28.0	182	1.36	1.06
N2437	07:41:41.0	-14:50:45.8	65	1.17	0.80
MarkA	20:43:39.6	-10:46:29.0	60	1.07	0.78
PG1323	13:25:45.0	-08:49:59.3	13	0.52	0.24

15 - 31 May

Beginning of the night: NGC2818 ($z \sim 1.05$), L98 ($z \sim 1.70$)
Middle of the night: E7
End of the night: E7

Suitable fields in this period:

Name	R.A. [hh:mm:ss]	DEC [±dd:mm:ss]	Nstars	$\Delta(B-V)$ [mag]	$\Delta(V-R)$ [mag]
Ru149	07:24:16.7	-00:32:20.1	207	1.21	0.86
E7	17:27:20.0	-45:02:28.0	182	1.36	1.06
L98	06:52:09.3	-00:19:00.3	165	1.38	1.05
N2818	09:16:22.9	-36:35:20.2	173	1.18	0.78
N6940	20:34:32.0	+28:15:10.0	90	1.12	0.77
MarkA	20:43:39.6	-10:46:29.0	60	1.07	0.78

01 - 14 June

Beginning of the night: E5 ($z \sim 1.09$), NGC2298 ($z \sim 1.87$)
Middle of the night: L110
End of the night: L110

Suitable fields in this period:

Name	R.A. [hh:mm:ss]	DEC [±dd:mm:ss]	Nstars	$\Delta(B-V)$ [mag]	$\Delta(V-R)$ [mag]
Ru149	07:24:16.7	-00:32:20.1	207	1.21	0.86
E7	17:27:20.0	-45:02:28.0	182	1.36	1.06
N2298	06:48:37.2	-35:58:34.6	126	1.23	0.88
N2818	09:16:22.9	-36:35:20.2	173	1.18	0.78
MarkA	20:43:39.6	-10:46:29.0	60	1.07	0.78
E5	12:05:13.3	-45:33:56.5	69	0.92	0.56
L110	18:42:46.1	+00:07:04.9	49	1.99	1.44

15 - 30 June

Beginning of the night: E5 ($z \sim 1.07$), NGC6121 ($z \sim 1.81$)

Middle of the night: NGC6121
End of the night: MarkA

Suitable fields in this period:

Name	R.A. [hh:mm:ss]	DEC [±dd:mm:ss]	Nstars	$\Delta(B-V)$ [mag]	$\Delta(V-R)$ [mag]
E7	17:27:20.0	-45:02:28.0	182	1.36	1.06
L98	06:52:09.3	-00:19:00.3	165	1.38	1.05
N2818	09:16:22.9	-36:35:20.2	173	1.18	0.78
N5139*	13:26:30.0	-47:10:23.0	100	1.12	0.60
MarkA	20:43:39.6	-10:46:29.0	60	1.07	0.78
N6940	20:34:32.0	+28:15:10.0	90	1.12	0.77
E5	12:05:13.3	-45:33:56.5	69	0.92	0.56
N6822*	19:44:53.0	-14:37:50.0	67	1.29	0.87
N6121*	16:24:10.0	-26:35:03.0	50	0.90	0.50

01 - 14 July

Beginning of the night: NGC5139 ($z \sim 1.08$), L101 ($z \sim 1.94$)
Middle of the night: PG1657
End of the night: MarkA

Suitable fields in this period:

Name	R.A. [hh:mm:ss]	DEC [±dd:mm:ss]	Nstars	$\Delta(B-V)$ [mag]	$\Delta(V-R)$ [mag]
E7	17:27:20.0	-45:02:28.0	182	1.36	1.06
N5139*	13:26:30.0	-47:10:23.0	100	1.12	0.60
N6940	20:34:32.0	+28:15:10.0	90	1.12	0.77
PG1657	16:59:35.5	+07:42:31.0	78	1.01	0.72
MarkA	20:43:39.6	-10:46:29.0	60	1.07	0.78
L101	09:56:53.0	-00:19:53.7	21	1.09	0.74

15 - 31 July

Beginning of the night: NGC5139 ($z \sim 1.10$), PG1047 ($z \sim 1.78$)
Middle of the night: PG1657
End of the night: PG2213

Suitable fields in this period:

Name	R.A. [hh:mm:ss]	DEC [±dd:mm:ss]	Nstars	$\Delta(B-V)$ [mag]	$\Delta(V-R)$ [mag]
E7	17:27:20.0	-45:02:28.0	182	1.36	1.06
N5139*	13:26:30.0	-47:10:23.0	100	1.12	0.60
NGC6940	20:34:32.0	+28:15:10.0	90	1.12	0.77
PG1657	16:59:35.5	+07:42:31.0	78	1.01	0.72
IC4499*	14:57:50.0	-82:12:00.0	41	0.45	0.27
PG2213	22:16:19.1	-00:21:14.1	22	0.88	0.64
PG1047	10:50:05.3	-00:00:57.4	14	0.77	0.50

01 - 14 August
Beginning of the night: NGC6121 ($z \sim 1.02$), IC4499 ($z \sim 1.87$)
Middle of the night: E7
End of the night: L95

Suitable fields in this period:

Name	R.A. [hh:mm:ss]	DEC [±dd:mm:ss]	Nstars	$\Delta(B-V)$ [mag]	$\Delta(V-R)$ [mag]
E7	17:27:20.0	-45:02:28.0	182	1.36	1.06
IC4499*	14:57:50.0	-82:12:00.0	41	0.45	0.27
N6940	20:34:32.0	+28:15:10.0	90	1.12	0.77
MarkA	20:43:39.6	-10:46:29.0	60	1.07	0.78
NGC6121*	16:24:10.0	-26:35:03.0	50	0.90	0.50
L107	15:39:32.7	-00:12:32.0	25	0.91	0.61
L95	03:53:38.7	+00:07:16.7	21	0.79	0.59

15 - 31 August
Beginning of the night: E7 ($z \sim 1.09$), E5 ($z \sim 1.81$)
Middle of the night: L110
End of the night: NGC2298

Suitable fields in this period:

Name	R.A. [hh:mm:ss]	DEC [±dd:mm:ss]	Nstars	$\Delta(B-V)$ [mag]	$\Delta(V-R)$ [mag]
E7	17:27:20.0	-45:02:28.0	182	1.36	1.06
NGC2298	06:48:37.2	-35:58:34.6	126	1.23	0.88
E5	12:05:13.3	-45:33:56.5	69	0.92	0.56
L110	18:42:46.1	+00:07:04.9	49	1.99	1.44
MarkA	20:43:39.6	-10:46:29.0	60	1.07	0.78
L95	03:53:38.7	+00:07:16.7	21	0.79	0.59
PG1323	13:25:45.0	-08:49:59.3	13	0.52	0.24

01 - 14 September
Beginning of the night: E7 ($z \sim 1.07$), NGC5139 ($z \sim 1.74$)
Middle of the night: MarkA
End of the night: NGC2298

Suitable fields in this period:

Name	R.A. [hh:mm:ss]	DEC [±dd:mm:ss]	Nstars	$\Delta(B-V)$ [mag]	$\Delta(V-R)$ [mag]
Ru149	07:24:16.7	-00:32:20.1	207	1.21	0.86
E7	17:27:20.0	-45:02:28.0	182	1.36	1.06
N2298	06:48:37.2	-35:58:34.6	126	1.23	0.88
MarkA	20:43:39.6	-10:46:29.0	60	1.07	0.78
N5139*	13:26:30.0	-47:10:23.0	100	1.12	0.60
IC4499*	14:57:50.0	-82:12:00.0	41	0.45	0.27
T-Phe	00:30:06.3	-46:28:08.6	14	1.00	0.71

15 - 30 September

Beginning of the night: E7 ($z \sim 1.11$), NGC6940 ($z \sim 1.95$)
Middle of the night: MarkA
End of the night: L98

Suitable fields in this period:

Name	R.A. [hh:mm:ss]	DEC [±dd:mm:ss]	Nstars	$\Delta(B-V)$ [mag]	$\Delta(V-R)$ [mag]
E7	17:27:20.0	-45:02:28.0	182	1.36	1.06
L98	06:52:09.3	-00:19:00.3	165	1.38	1.05
N2298	06:48:37.2	-35:58:34.6	126	1.23	0.88
NGC6940	20:34:32.0	+28:15:10.0	90	1.12	0.77
MarkA	20:43:39.6	-10:46:29.0	60	1.07	0.78
PG2213	22:16:19.1	-00:21:14.1	22	0.88	0.64
T-Phe	00:30:06.3	-46:28:08.6	14	1.00	0.71

01 - 14 October

Beginning of the night: MarkA ($z \sim 1.05$), PG1633 ($z \sim 1.96$)
Middle of the night: PG2213
End of the night: Ru149

Suitable fields in this period:

Name	R.A. [hh:mm:ss]	DEC [±dd:mm:ss]	Nstars	$\Delta(B-V)$ [mag]	$\Delta(V-R)$ [mag]
Ru149	07:24:16.7	-00:32:20.1	207	1.21	0.86
N6940	20:34:32.0	+28:15:10.0	90	1.12	0.77
N6822*	19:44:53.0	-14:37:50.0	67	1.29	0.87
MarkA	20:43:39.6	-10:46:29.0	60	1.07	0.78
PG1633	16:35:12.1	+09:50:59.0	60	0.92	0.61
PG2213	22:16:19.1	-00:21:14.1	22	0.88	0.64
L95	03:53:38.7	+00:07:16.7	21	0.79	0.59

15 - 31 October

Beginning of the night: MarkA ($z \sim 1.03$), NGC6121 ($z \sim 2.02$)
Middle of the night: L95
End of the night: NGC2818

Suitable fields in this period:

Name	R.A. [hh:mm:ss]	DEC [±dd:mm:ss]	Nstars	$\Delta(B-V)$ [mag]	$\Delta(V-R)$ [mag]
Ru149	07:24:16.7	-00:32:20.1	207	1.21	0.86
N2818	09:16:22.9	-36:35:20.2	173	1.18	0.78
N6940	20:34:32.0	+28:15:10.0	90	1.12	0.77
MarkA	20:43:39.6	-10:46:29.0	60	1.07	0.78
N6121*	16:24:10.0	-26:35:03.0	50	0.90	0.50
L95	03:53:38.7	+00:07:16.7	21	0.79	0.59
L92	00:55:09.7	+00:42:49.9	19	0.66	0.42

01 - 14 November

Beginning of the night: MarkA ($z \sim 1.11$), NGC6940 ($z \sim 1.89$)
Middle of the night: E3
End of the night: NGC2818

Suitable fields in this period:

Name	R.A. [hh:mm:ss]	DEC [±dd:mm:ss]	Nstars	$\Delta(B-V)$ [mag]	$\Delta(V-R)$ [mag]
N2818	09:16:22.9	-36:35:20.2	173	1.18	0.78
N6940	20:34:32.0	+28:15:10.0	90	1.12	0.77
L110	18:42:46.1	+00:07:04.9	49	1.99	1.44
MarkA	20:43:39.6	-10:46:29.0	60	1.07	0.78
E3	06:43:13.6	-45:13:28.8	39	0.93	0.60
T-Phe	00:30:06.3	-46:28:08.6	14	1.00	0.71

15 - 30 November

Beginning of the night: T-Phe ($z \sim 1.11$), PG0231 ($z \sim 1.76$)
Middle of the night: NGC2298
End of the night: NGC2298

Suitable fields in this period:

NAME	R.A. [hh:mm:ss]	DEC [±dd:mm:ss]	Nstars	$\Delta(B-V)$ [mag]	$\Delta(V-R)$ [mag]
L98	06:52:09.3	-00:19:00.3	165	1.38	1.05
N2298	06:48:37.2	-35:58:34.6	126	1.23	0.88
L95	03:53:38.7	+00:07:16.7	21	0.79	0.59
T-Phe	00:30:06.3	-46:28:08.6	14	1.00	0.71
PG0231	02:33:40.9	+05:19:15.0	12	0.78	0.45

01 - 14 December

Beginning of the night: T-Phe ($z \sim 1.08$), MarkA ($z \sim 1.86$)
Middle of the night: Ru149
End of the night: NGC2298

Suitable fields in this period:

Name	R.A. [hh:mm:ss]	DEC [±dd:mm:ss]	Nstars	$\Delta(B-V)$ [mag]	$\Delta(V-R)$ [mag]
Ru149	07:24:16.7	-00:32:20.1	207	1.21	0.86
L98	06:52:09.3	-00:19:00.3	165	1.38	1.05
N2298	06:48:37.2	-35:58:34.6	126	1.23	0.88
MarkA	20:43:39.6	-10:46:29.0	60	1.07	0.78
L95	03:53:38.7	+00:07:16.7	21	0.79	0.59
T-Phe	00:30:06.3	-46:28:08.6	14	1.00	0.71

15 - 31 December

Beginning of the night: T-Phe ($z \sim 1.12$), PG2213 ($z \sim 1.81$)
Middle of the night: NGC2298

End of the night: L98

Suitable fields in this period:

Name	R.A.	DEC	Nstars	$\Delta(B - V)$	$\Delta(V - R)$
	[hh:mm:ss]	[±dd:mm:ss]		[mag]	[mag]
T-Phe	00:30:06.3	-46:28:08.6	14	1.00	0.71
N2298	06:48:37.2	-35:58:34.6	126	1.23	0.88
L98	06:52:09.3	-00:19:00.3	165	1.38	1.05
Ru149	07:24:16.7	-00:32:20.1	207	1.21	0.86
PG2213	22:16:19.1	-00:21:14.1	22	0.88	0.64

Appendix A

The FORS2 pipeline recipe `fors_photometry` may be used to simultaneously process multiple photometric tables produced by the recipe `fors_zeropoint`. The purpose of the recipe is to fit a user-configurable photometric model to the set of instrumental magnitude measurements of the standard stars (and non-standard stars if required) and to return the values of the fitted coefficients to enable the user to photometrically calibrate their science object photometry. The photometric model in `fors_photometry` may be configured to include various combinations of terms corresponding to the photometric zero point, linear atmospheric extinction terms, linear colour terms, and two-dimensional spatial polynomial terms. In particular, `fors_photometry` is capable of fitting the photometric model represented by Equation 1.

We performed the standard verification work for `fors_photometry` as described in Section 2 and we found that the recipe functions correctly as described in the pipeline manual. The most important of these verifications consisted of testing the fits performed by the recipe. For each possible combination of photometric parameters that may be fit with `fors_photometry` (or in other words, for each available photometric model), we generated a set of photometric tables containing fake noiseless instrumental magnitude measurements. This was done by adopting the standard star entries from a set of real photometric tables produced by `fors_zeropoint` and then transforming the corresponding standard magnitudes to instrumental magnitudes using the adopted photometric model and its coefficients. We then used `fors_photometry` to fit the fake instrumental magnitude measurements with the adopted photometric model and we compared the fitted values for the coefficients with the values used to generate the fake data. We found that the fitted values of the coefficients matched the values used to generate the fake data to within numerical precision for *all* available types of photometric model in `fors_photometry`. Hence we conclude that the fitting method is robust and reliable.

We also tested fitting a subset of the available photometric models in `fors_photometry` to fake noisy instrumental magnitude measurements. We did this in the same way as for the fake noiseless instrumental magnitude measurements, except that we used the magnitude uncertainties listed in the real photometric tables to generate random Gaussian noise that we added to the fake instrumental magnitude measurements. We then used `fors_photometry` to fit the instrumental magnitude measurements as before with the current photometric model under consideration to yield noisy fitted values for the model coefficients. Repeating this procedure 1000 times enabled us to verify that the reported uncertainties on the fitted values for the model coefficients match the observed scatter in these coefficients as measured over the 1000 simulations, and that the mean values of the fitted model coefficients match the values used to generate the fake data to within the uncertainty on the mean. Hence we conclude that `fors_photometry` reports reliable uncertainties on the fitted photometric parameters, and that when the correct photometric model is chosen, `fors_photometry` does not introduce any biases into the fitted values of the photometric parameters.

During our verification work, we were presented with the opportunity to perform a detailed comparison with similar independent software written in IDL by ourselves via the `DanIDL` module `fit_photometric_calibration.pro`. For each available photometric model in `fors_photometry`, we verified that fits using `fors_photometry` and `fit_photometric_calibration.pro` on exactly the same data yielded fitted values of the model coefficients that matched to within ∼1% in most cases, and regularly matched to within ∼0.1%. The slight differences that do exist in the fitted values may be traced to the different data weighting schemes used by `fors_photometry` and `fit_photometric_calibration.pro`, where `fors_photometry` implements a full treatment of covariance
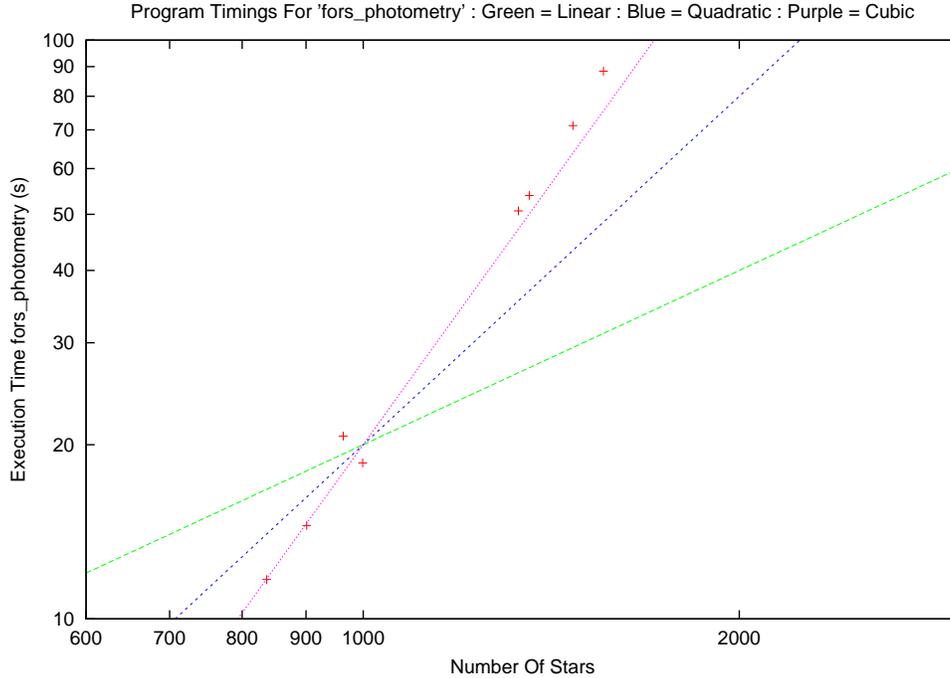
Figure 12: Plot of processing time (s) as a function of the number of instrumental magnitude measurements of standard stars using the FORS2 pipeline recipe fors_photometry. Red plus-signs represent actual measurements of the processing time, and the green, blue and purple straight lines serve to illustrate the gradients of linear, quadratic and cubic functions, respectively, on this log-log-scale plot.

via the construction of the *design matrix* in the linear least squares problem, and fit_photometric_calibration.pro ignores covariance via construction of the *normal equations* in the linear least squares problem (see Press et al. 2007). This is of course a very encouraging result, although it highlights the fact that the extra coding effort in dealing with error covariance may not have been necessary to obtain an accurate fit.

We also note that fors_photometry (as opposed to fit_photometric_calibration.pro) has not been designed to simultaneously fit more than one photometric zero point, and consequently FORS2 data from each detector must be treated separately in order to determine an estimate of the photometric zero point for each detector. This situation results in separate estimates of the extinction coefficient for each night from the data for each detector. This may be viewed as an advantage since multiple estimates of the extinction coefficient for each night provide a consistency check on the results. However, for N nights of observation and two detectors this results in fitting a total of $2N + 4$ parameters to the data. Adopting a single, more comprehensive, photometric model consisting of two photometric zero points, nightly extinction coefficients and a single colour term coefficient requires the fitting of only $N + 3$ parameters to the same data, and consequently, the precision of the fitted extinction coefficients will be substantially better in this case.

We identified one disadvantage with fors_photometry when processing large data sets of >5000 magnitude measurements. The processing time for such data sets is of the order of hours to days, and the processing time is proportional to N_d^3, where N_d is the number of instrumental magnitude measurements that are being fitted (see Figure 12). Hence, large data sets, typical of fits spanning multiple nights of observation, can quickly become intractable to perform with available computing power. Smaller data sets have more reasonable processing times (e.g. $\sim$20 s for $N_d \sim$1000, $\sim$10.5 min for $N_d \sim$3000, $\sim$49 min for $N_d \sim$5000, etc.). However, we note that the program fit_photometric_calibration.pro runs *much* faster, processing 1000 magnitude measurements in just $\sim$0.01 s. This is again due to the different approaches to the solution of the linear least squares problem taken by the different programs. The design matrix constructed by fors_photometry is a rectangular matrix of size $N_p \times N_d$ elements (where N_p is the number of parameters in the photometric model) which is much larger than the

$N_p \times N_p$ matrix for the normal equations constructed by `fit_photometric_calibration.pro`, since typically $N_d \gg N_p$, and the larger size leads to a much longer solution time. We note that when N_d is especially large, the design matrix cannot fit in the computer memory, and currently this limit is reached by `fors_photometry` running on QC computers when performing a fit of the standard star photometric data for a single period (*DFS09688* - SUSPENDED). In contrast, the program `fit_photometric_calibration.pro` does not suffer from this memory problem.

We summarise our findings relating to `fors_photometry` as follows:

1. The recipe has a well-designed and well-documented interface, and we did not find any problems with the input parameters.

2. The fitting method implemented in the recipe is robust and reliable.

3. The recipe reports reliable uncertainties on the fitted parameters.

4. The results produced by the recipe are consistent with corresponding results provided by independent software.

5. The recipe cannot fit a photometric model that includes more than one photometric zero point, which corresponds to the case where data includes photometry from multiple detectors.

6. The full covariance error propagation implemented in the recipe, which requires the construction of a design matrix in the solution of the linear least squares problem, produces fitted parameter values that differ very little ($\sim$0.1%) from those derived ignoring the treatment of covariance via the construction of the normal equations and implemented in `fit_photometric_calibration.pro`. However, the `fors_photometry` recipe runs $\sim$2000 times slower than `fit_photometric_calibration.pro` and with much greater memory requirements, limiting the usefulness of this recipe for larger data sets ($>$5000 magnitude measurements).

Appendix B

The current (July 2011) calibration plan in operation at Paranal is as follows:

```
Calibration: Photometric Standard Star Field in BVRI
Validity:    1 Day
Template/OB: FORS2_img_obs_crsplit
Usage:
Standards must be taken from the following queues: FORS1-Photom-std or
FORS2-Photom-std. Photometric standard should be taken to measure the
zero-points for the night to determine if the night is photometric.
Photometric standard should be taken each night when the conditions
are clear/photometric. However, note that according to the manual this
is mandatory only for PHO conditions, so there is not reason to
classifiy imaging observations in CLR and without standard as "C".
These OBs only contain BVRI. OBs are prepared. Note: for COLL_HR the
collimator MUST be set in BOB!


Calibration: Photometric Standard Star at High Airmass
Validity:    1 Day
Template/OB: FORS2_img_obs_crsplit (with SEQ.CATG=STANDARD)
Usage:
According to the calibration plan the high airmass standards must be
taken in the standard settings to distinguish between atmospheric
extinction and instrumental zero points. The plan is to observe the
BVRI sequence for one of the Stetson fields at 2.3 > airmass > 1.6
whenever imaging observations are done in a clear or photometric
night in Service Mode.
```

Appendix C

The contents of the proposed offset files for standard star observations as referred to in the last column of Table 1 are reproduced here:

```
# offset pattern for standard star observations
# offsets in arcsec  rotation in degree

# offsets_0.dat
#
#   X          Y              rot
     0          0              0
   -00        -00             90
   -00        -00            180
   -00        -00            270


# offsets_1.dat
#
#   X          Y              rot
     0          0              0
   -60        -60              0
    60        -60              0
   -60         60              0
    60         60              0
   -60        -60            180
    60        -60            180
   -60         60            180
    60         60            180
   -60        -60             90
    60        -60             90
   -60         60             90
    60         60             90
   -60        -60            270
    60        -60            270
   -60         60            270
    60         60            270
   -60          0              0
    60          0              0
     0        -60              0
     0         60              0
     0          0            180
   -60          0            180
    60          0            180
     0        -60            180
     0         60            180
     0          0             90
   -60          0             90
    60          0             90
     0        -60             90
     0         60             90
     0          0            270
   -60          0            270
```

```
    60          0           270
     0        -60           270
     0         60           270


# offsets_2.dat
#
#   X          Y            rot
     0          0            0
   -10        -10            0
    10        -10            0
   -10         10            0
    10         10            0
   -10        -10          180
    10        -10          180
   -10         10          180
    10         10          180
   -10        -10           90
    10        -10           90
   -10         10           90
    10         10           90
   -10        -10          270
    10        -10          270
   -10         10          270
    10         10          270
   -10          0            0
    10          0            0
     0        -10            0
     0         10            0
     0          0          180
   -10          0          180
    10          0          180
     0        -10          180
     0         10          180
     0          0           90
   -10          0           90
    10          0           90
     0        -10           90
     0         10           90
     0          0          270
   -10          0          270
    10          0          270
     0        -10          270
     0         10          270


# offsets_3.dat
#
#   X          Y            rot
     0          0            0
   -30        -30            0
    60        -30            0
   -30         60            0
```

60	60	0
-30	-10	180
60	-10	180
-30	60	180
20	20	180
-20	-20	90
20	-20	90
-20	20	90
20	20	90
-20	-20	270
20	-20	270
-20	20	270
20	20	270
-30	0	0
60	0	0
0	-30	0
0	60	0
0	0	180
-30	0	180
60	0	180
0	-20	180
0	60	180
0	0	90
-20	0	90
20	0	90
0	-20	90
0	60	90
0	0	270
-20	0	270
20	0	270
0	-20	270
0	20	270

Acknowledgements

References

Bertin E. & Arnouts S., 1996, A&ASS, 117, 393

Bramich D.M. & Freudling W., 2012, Report: Preparation Of The UVES Pipeline For The `Reflex` Release, VLT-TRE-SO-19500-5385, Issue 2.0

Møller P. et al., 2005, FORS: An Assessment Of Obtainable Photometric Accuracy And Outline Of Strategy For Improvement, VLT-TRE-ESO-13100-3808, Issue 1

Moehler S. et al., 2010, PASP, 122, 93

Freudling W. et al., 2006, The FORS Absolute Photometry Project, VLT-TRE-ESO-13100-4006, Issue 1.1

Freudling W. et al., 2007, ASP Conference Series: The Future Of Photometric, Spectrophotometric And Polarimetric Standardization, 364, 113

Freudling W. & Bramich D.M., 2009, Internal Memorandum: QC Of FORS Photometric Parameters

Freudling W., Bramich D.M. & Møller P., 2011, Internal Memorandum: FORS Rotation Angle Uncertainties

Izzo C., de Bilbao L. & Larsen J.M., 2011, FORS Pipeline User Manual, VLT-MAN-ESO-19500-4106, Issue 4.1

Pál A. & Bakos G.Á., 2006, PASP, 118, 1474

Press W.H. et al., 2007, Numerical Recipes: The Art Of Scientific Computing, Third Edition, p788-791

Saviane I., 2010, FORS User Manual, VLT-MAN-ESO-13100-1543, Issue 87.0

Silva D., 2007, Phase 2 Proposal Preparation Tool (P2pp) User Manual, VLT-MAN-ESO-19200-1644, Issue 9

Stetson P.B., 2000, PASP, 112, 925

Stetson P.B., 2007, Stetson Photometric Standard Fields,
http://www3.cadc-ccda.hia-iha.nrc-cnrc.gc.ca/community/STETSON/standards/

Valdes F.G. et al., 1995, PASP, 107, 1119